Materials Advances

ROYAL SOCIETY OF CHEMISTRY

PAPER

View Article Online
View Journal | View Issue

Cite this: *Mater. Adv.*, 2024, 5, 3863

Entanglement of cation ordering and manipulation of the magnetic properties through a temperature-controlled topotactic interface reaction in nanocomposite perovskite oxides†

Sudipa Bhattacharya,[a] Radhamadhab Das,[a] Shreyashi Chowdhury,[a] K. K. Supin,[bc] M. Vasundhara,*[bc] Jyoti Ranjan Sahu,[d] Trilochan Bhunia,[e] Arup Gayen,[e] Oleg I. Lebedev[f] and Md. Motin Seikh*[a]

Received 21st October 2023,
Accepted 11th March 2024

DOI: 10.1039/d3ma00891f

rsc.li/materials-advances

Achievement of B-site cation ordering for $LaFe_{0.5}Mn_{0.5}O_3$, unlike other $LaB_{0.5}B'_{0.5}O_3$ perovskites, has not been reported yet in polycrystalline samples. Thus far, there has been only one report on Fe and Mn ordering in $LaMnO_3$–$LaFeO_3$ artificial superlattices constructed on $SrTiO_3$ using laser MBE methods [Ueda *et al. Phys. Rev. B*, 1999, **60**, R12561.]. The ferromagnetic ordering with the T_C around 230 K has been attributed to the $Fe^{3+}(d^5)$–O–$Mn^{3+}(d^4)$ superexchange interaction for the superlattice with 1/1 stacking periodicity. Here, for the first time, we report the Fe and Mn ordering at the interface of the $La_{0.45}Ca_{0.55}MnO_3$–$LaFeO_3$ (LCMO–LFO) nanocomposite, achieving a T_C of ~225 K. It has been also observed that such an ordering is very sensitive to the processing temperature. Processing the composite at 1000 °C leads to complete randomization in the cationic distribution, which results in suppression of the high temperature transition at 225 K observed for 700 and 800 °C heat-treated samples. High-resolution TEM, HAADF, EDX mapping and ED analysis support the interfacial phase formation. This cationic ordering through interfacial reaction is further substantiated by the formation of a well-studied La_2MnCoO_6 double perovskite obtained from a $LaMnO_3$–$LaCoO_3$ nanocomposite by thermal treatment under similar conditions as that of the LCMO–LFO system. Our study revealed that by means of the interface reaction during composite processing, the product phase may dominate the overall property of the system. The temperature-controlled cationic ordering at the interfacial product phase of dominating magnetic properties may provide a novel route to design functional ceramic materials.

Introduction

The most popular advantage of composite materials is their improved structural functionalities such as specific strength, creep and fatigue behaviour, wear resistance, and damping properties for engineering applications.[1–3] The structural integrity and mechanical behaviour of composite materials are sensitive to the chemical compatibility between reinforcement and a matrix. The chemical compatibility is demonstrated by interfacial reaction between the components, which is generally avoided due to loss of the reinforcement, as well as possible formation of a brittle intermetallic product phase. Thus, it is desirable to circumvent the interfacial reaction. The reinforcement should chemically wet the matrix to establish chemical bonding strength, as well as minimize interfacial energy. However, the multiphase composite materials behave as an interfacial material. Consequently, their performance depends on the characteristics of internal interfaces.[4–7] The polycrystalline solids consist of a large number of interfaces that are full of diverse non-periodic atomic structures. Thus, a detailed description and fundamental understanding of interfaces and their influence on the macroscopic properties of solids are really a formidable task. A matrix and reinforcement may result in a thermodynamically compatible composite member by an intentional reaction at a local interface area through *in situ* processing.[5,8,9] For the formation of an intermediate phase at

[a] *Department of Chemistry, Visva-Bharati University, Santiniketan–731235, West Bengal, India. E-mail: mdmotin.seikh@visva-bharati.ac.in*
[b] *Polymers and Functional Materials Department, CSIR-Indian Institute of Chemical Technology, Hyderabad-500007, India. E-mail: mvas@iict.res.in*
[c] *Academy of Scientific and Innovative Research (AcSIR), Ghaziabad-201002, India*
[d] *P.G. Department of Physics, Maharaja Sriram Chandra Bhanja Deo University, Baripada-757003, India*
[e] *Department of Chemistry, Jadavpur University, Kolkata 700032, India*
[f] *Laboratoire CRISMAT, ENSICAEN UMR6508, 6 Bd Maréchal Juin, Cedex 4, Caen-14050, France*

† Electronic supplementary information (ESI) available. See DOI: https://doi.org/10.1039/d3ma00891f

the interface, the composite members experience a compositional change through the phase equilibria and diffusion pathways.[10–12] The produced intermediate phase may play a crucial role in determining the properties of the composite phase.

The customization of the physical properties of an electronically correlated oxide nanocomposite system is nontrivial. This is because of the complex nature of the individual components, which exhibits intriguing physical properties associated with the strong electronic correlation. Such complexity is further augmented when the particle size is reduced to the nanoscale.[13–16] The materials with combined functionality are of interest for various practical applications. Composite materials can provide such functionality based on the product property where the cross-correlated electronic and magnetic properties can serve the purpose.[17,18] The product property (such as magnetoelectric coupling) can be achieved from the composite of magnetostrictive and piezoelectric phases.[17,19,20] There are numerous studies that have shown modification of physical properties in correlated functional oxides nanocomposites.[21–30] The optimized interface between the hard ($SrFe_{12}O_{19}$) and soft ($CoFe_2O_4$) magnetic phases results from symbiotic grain growth, where one phase helps in the crystallization of the other one in the sol–gel process through the strong interfacial magnetic coupling between the two phases.[29] A decrease in a magnetic moment with an increase in the coercive field of $La_{0.7}Sr_{0.3}MnO_3$ is observed in the $La_{0.7}Sr_{0.3}MnO_3/NiFe_2O_4$ core–shell structure.[21] The morphology-dependent magnetic coupling has been reported for the $La_{0.7}Ca_{0.3}MnO_3/CoFe_2O_4$ nanocomposite.[22] The magnetic proximity effects and interface exchange interactions are reported to change the ferromagnetic T_C by ~50 K for $SrFe_{12}O_{19}$ and $La_{0.7}Sr_{0.3}MnO_3$ in composite with $CaCu_3Ti_4O_{12}$.[25] For oxide nanocomposite systems, the proper choice of a second phase can be used to tune the magnetic properties of the matrix.[27] A dramatic change in the magnetic properties of the multiferroic double perovskite La_2MnCoO_6 in composite with $CaCu_3Ti_4O_{12}$ is observed due to local structural modification across the grain boundary.[26] The interfacial interaction between the Fe_3O_4 nanoparticles and reduced graphene oxide nanosheets is reported to exhibit high performance as an anode material for lithium-ion batteries.[31] However, the effect of the temperature-dependent interfacial reaction between the nanocomposites to modify their properties has not been explored in detail.

In this manuscript, we have explored the potential of the temperature-controlled interface reaction to control the cationic ordering for developing functional materials. The creation of new materials with unique physical properties can be achieved through the superlattice deposition by controlled atomic ordering in the film plane.[32–34] Theoretical calculations revealed the A-type antiferromagnetic (A-AFM) ordering at the interface of the $SrCrO_3/YCrO_3$ superlattice where $SrCoO_3$ and $YCrO_3$ are of C-AFM and G-AFM, respectively, and it becomes ferromagnetic under a compressive strain of 1%.[35] In this regard, it is worth mentioning the atomic ordering in $LaMnO_3$–$LaFeO_3$ artificial superlattices constructed on $SrTiO_3$ using laser MBE methods.[36] The magnitude of magnetization increases with the increase in the number of Fe–Mn interfaces. The superlattice with 1/1 stacking periodicity shows ferromagnetic ordering with the T_C around 230 K.[36] These ferromagnetic interactions at the $LaMnO_3$–$LaFeO_3$ interfaces have been attributed to the $Fe^{3+}(d^5)$–O–$Mn^{3+}(d^4)$ superexchange, according to the Goodenough–Kanamori rule.[37,38] However, the partial displacement between Fe and Mn with the decrease in the number of $LaMnO_3$–$LaFeO_3$ interfaces results in reduced magnetization, which corresponds to the antisite disordering, as observed in La_2MnMO_6 (M = Co and Ni).[39–42] The observation of long range ferromagnetic ordering in $LaMn_{0.5}Fe_{0.5}O_3$ through the $Fe^{3+}(d^5)$–O–$Mn^{3+}(d^4)$ superexchange interaction, which is achieved by cationic ordering across the $LaMnO_3$–$LaFeO_3$ interface in a thin film is of significant importance. This is because of the fact that polycrystalline $LaMn_{0.5}Fe_{0.5}O_3$ fails to exhibit long range spin ordering, unlike other $LaB_{0.5}B'_{0.5}O_3$ compositions.[43–46] $LaMn_{0.5}Cr_{0.5}O_3$, $LaMn_{0.5}Co_{0.5}O_3$ and $LaMn_{0.5}Ni_{0.5}O_3$ exhibit the ferromagnetic T_C at around 120, 225 and 280 K, respectively,[41,42,47–50] whereas $LaCo_{0.5}Fe_{0.5}O_3$, $LaCo_{0.5}Cr_{0.5}O_3$ and $LaFe_{0.5}Ni_{0.5}O_3$ are antiferromagnetic with the T_N 370, 295 and ~100 K, respectively.[51–53] However, $LaMn_{0.5}Fe_{0.5}O_3$ with uniform Fe and Mn distribution was found to be of nonmagnetic behavior, where cluster-like ferromagnetic or antiferromagnetic states appear for inhomogeneous cationic distribution.[54–56] Even the hole-doped $La_{1-x}A_xFe_{0.5}Mn_{0.5}O_3$ (A = Ca, Sr, Ba and Pb) with altered valence in the B-site failed to manifest the long-range ordering.[57,58] On the other hand, the magnetic properties of $LaMn_{0.5}Fe_{0.5}O_3$ are very much sensitive to the synthesis conditions and annealing temperatures, resulting in controversial magnetic states, particularly in nanostructured form.[46,59,60]

Here, we observed that atomic ordering of $Fe^{3+}(d^5)$ and $Mn^{3+}(d^4)/Mn^{4+}(d^3)$ takes place at the interface of the composite made up from $La_{0.45}Ca_{0.55}MnO_3$ and $LaFeO_3$. The cation ordered phase exhibits a magnetic transition at ~225 K in agreement with the reported thin film. Such ordering is sensitive to the thermal treatment. For the 700 and 800 °C annealed samples, such ordering prevailed. However, for the 1000 °C annealed samples, a uniform distribution of $Fe^{3+}(d^5)$ and $Mn^{3+}(d^4)/Mn^{4+}(d^3)$ takes place with the formation of the nonmagnetic single phase $La_{0.725}Ca_{0.275}Mn_{0.5}Fe_{0.5}O_3$ composition. Such cation ordering due to the interface reaction is substantiated from a similar study on the $LaMnO_3$–$LaCoO_3$ nanocomposite, which results in the formation of the well-known double perovskite La_2MnCoO_6 with a T_C of 220 K. This result demonstrates the temperature-controlled evolution of the product phase from the topotactic reaction at the interface of the nanocomposite for novel functionality.

Experimental details

The composites $(La_{0.45}Ca_{0.55}MnO_3)_{1-x}(LaFeO_3)_x$ (where, x = 0, 0.5 and 1.0) were fabricated by intimate mixing of the two individual pure phase components, $La_{0.45}Ca_{0.55}MnO_3$ and $LaFeO_3$, followed by heating at different temperatures. The individual

components $La_{0.45}Ca_{0.55}MnO_3$ and $LaFeO_3$ in their nanodimension were chemically synthesized *via* conventional sol–gel self-combustion synthesis technique using citric acid as a gelling agent. For the preparation of nanostructured $LaFeO_3$ and $La_{0.45}Ca_{0.55}MnO_3$, a stoichiometric ratio of metal nitrate salts $La(NO_3)_3{\cdot}6H_2O$ (Alfa Aesar, 99.9%), $Fe(NO_3)_3{\cdot}9H_2O$ (Alfa Aesar, 99.9%) [for $LaFeO_3$] and $La(NO_3)_3{\cdot}6H_2O$ (Alfa Aesar, 99.9%), $Ca(NO_3)_2{\cdot}4H_2O$ (Sigma Aldrich, 99.9%) and $Mn(OAc)_2{\cdot}4H_2O$ (99.5%, Merck) [for $La_{0.45}Ca_{0.55}MnO_3$] were dissolved in 50 mL double-distilled water. About 2 mL of conc. nitric acid was added to prevent the hydrolysis of the aquated metal ions. The reaction mixture was stirred for 2 h using a magnetic stirrer, followed by the addition of citric acid at about four times the mole ratio of the metal ions until a homogeneous, clear solution was obtained. The resulting solution was then stirred at 60 °C for 6 h, followed by evaporation at 90 °C to form the gel. The gel was dried at 150 °C and the resulting crude was ground thoroughly using an agate mortar-pestle, and then heated in air at 500 °C for 10 h and 15 h to obtained fine powders of $LaFeO_3$ and $La_{0.45}Ca_{0.55}MnO_3$, respectively. The $La_{0.45}Ca_{0.55}MnO_3$–$LaFeO_3$ composite was prepared by physical mixing of equimolar $La_{0.45}Ca_{0.55}MnO_3$ and $LaFeO_3$ in a mortar-pestle with ethanol to obtain a fine mixture of the two pristine phases. Then, this equimolar composite was divided into four parts to anneal at different temperatures, more specifically at 600, 700, 800 and 1000 °C for 10 h.

A Bruker D8 Advance X-ray diffractometer operating at 40 kV and 40 mA with Cu K_α radiation (λ = 1.5418 Å) was used to record the powder X-ray diffraction (PXRD) patterns. The data were collected in the 2θ range of 10°–100° using the LYNXEYE detector (1D mode) with a dwell time of 1 s per step. A *Zeiss GeminiSEM 450* field emission scanning electron microscope (FE-SEM), operated at an accelerating voltage of 20 kV, was used for imaging the sample surface morphology, to determine the particle size, energy dispersive X-ray analysis (EDX) and elemental mapping. Transmission electron microscopy (TEM), including electron diffraction (ED), high-angle annular dark-field scanning TEM (HAADF-STEM), and simultaneously acquired energy dispersive X-ray (EDX) elemental mapping experiments were carried out on an aberration double-corrected cold FEG JEM ARM200F microscope operated at 200 kV and equipped with a CENTURIO EDX detector, ORIUS Gatan camera and Quantum GIF. For all of the samples, X-ray photoelectron spectroscopy (XPS) measurements were carried out on the powder form at room temperature. The XPS spectra were recorded using a PHI 5000 Versa Probe II, ULVAC-PHI, Inc. instrument using Al Ka1 as the X-ray source. During the measurement time, the XPS chamber pressure was maintained at 5×10^{-10} mbar. The binding energy (B.E.) of the elements was corrected by C 1s as the reference energy (C 1s = 284.8 eV). A wide scan was performed to detect the presence of total elements in the sample surface, which confirms the purity of the samples as well. The high-resolution scans of the

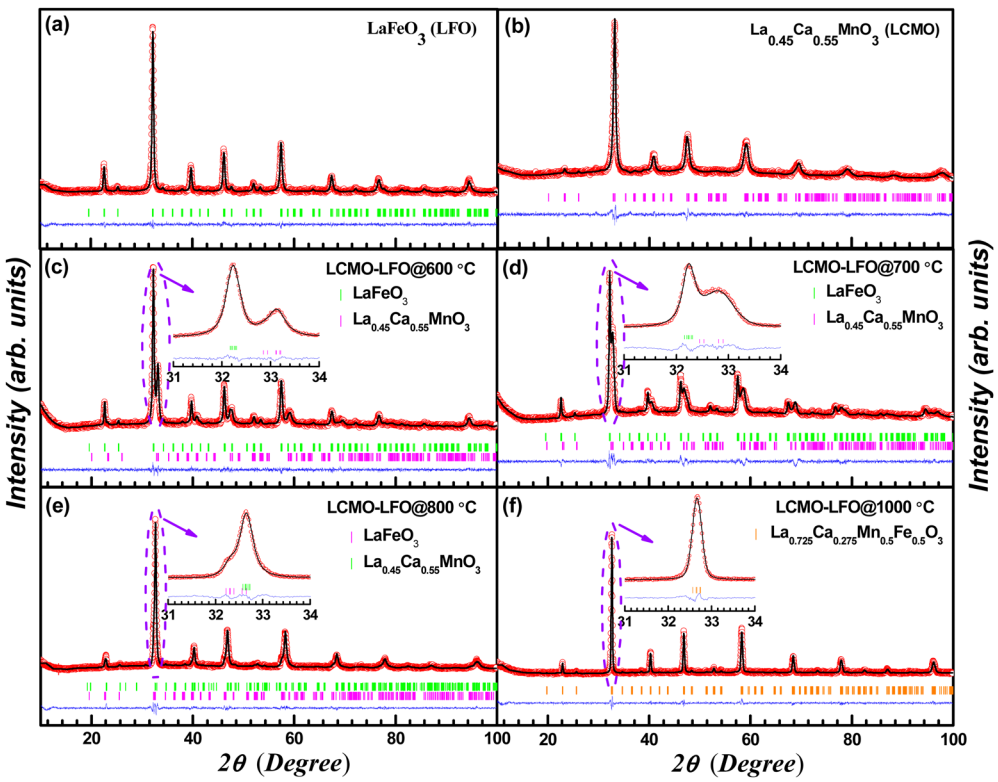

Fig. 1 Powder X-ray diffraction patterns of (a) $LaFeO_3$ (LFO), (b) $La_{0.45}Ca_{0.55}MnO_3$ (LCMO) and LCMO–LFO composite annealed at: (c) 600 °C, (d) 700 °C, (e) 800 °C and (f) 1000 °C. Insets in (c)–(f) show the enlarged view between 31–34°, confirming the presence of LCMO and LFO at 800 °C and single phase $La_{0.725}Ca_{0.275}Mn_{0.5}Fe_{0.5}O_3$ formation at 1000 °C. The open red circles, black lines, the bottom blue lines and vertical bars represent the experimental data, calculated pattern, difference curve and Bragg position, respectively.

Table 1 The refinement and structural parameters, along with the bond lengths and bond angles, for the $La_{0.45}Ca_{0.55}MnO_3$ (LCMO), $LaFeO_3$ (LFO) and LCMO–LFO composites annealed at different temperatures

Composition and phase	Lattice parameters	Bond distance (Å)	Bond angle (°)	Atomic coordinates			
				Atom	x	y	z
$La_{0.45}Ca_{0.55}MnO_3$ $La_{0.45}Ca_{0.55}MnO_3$ Orthorhombic (S.G. P*bnm*)	a = 5.405 (7) Å	1 × Ca_1/La_1–O_1: 2.4353(3)	∠Mn_1–O_1–Mn_1: 162.133(3)	La	0.50604(3)	0.51900(2)	0.25000(0)
	b = 5.398 (0) Å	1 × Ca_1/La_1–O_1: 2.6181(4)	∠Mn_1–O_2–Mn_1: 164.322(3)	Ca	0.50604(1)	0.51900(2)	0.25000(1)
	c = 7.688 (4) Å	2 × Ca_1/La_1–O_2: 2.4844(2)		Mn	0.50000(2)	0.00000(0)	0.00000(1)
	V = 224.352(5) Å^3	2 × Ca_1/La_1–O_2: 2.6489(2)		O1	0.44410(2)	0.00000(1)	0.25000(3)
	R_b = 1.80	2 × Mn_1–O_1: 1.9456(2)		O2	0.74640(5)	0.29440(2)	0.02420(2)
	R_f = 1.80	2 × Mn_1–O_2: 1.7736(2)					
	χ^2 = 1.68	2 × Mn_1–O_2: 2.0817(2)					
$LaFeO_3$ Orthorhombic (S.G. P*bnm*)	a = 5.556(0) Å	2 × La_1–O_1: 2.4496(2)	∠Fe_1–O_1–Fe_1: 157.084(5)	La	0.99300(5)	0.02970(1)	0.25000(2)
	b = 5.568(4) Å	2 × La_1–O_1: 2.6920(2)	∠Fe_1–O_2–Fe_1: 154.031(3)	Fe	0.00000(0)	0.50000(2)	0.00000(1)
	c = 7.845(6) Å	1 × La_1–O_2: 2.3855(3)		O1	0.71900(5)	0.30200(2)	0.02900(0)
	V = 242.737(6) Å^3	1 × La_1–O_2: 2.5810(4)		O2	0.08000(0)	0.48500(4)	0.25000(1)
	R_b = 2.26	2 × Fe_1–O_1: 1.9248(2)					
	R_f = 2.81	2 × Fe_1–O_1: 2.0882(3)					
	χ^2 = 1.13	2 × Fe_1–O_2: 2.0127(2):					
LCMO–LFO @600 °C $LaFeO_3$ phase Orthorhombic (S.G. P*bnm*)	a = 5.555(4) Å	2 × La_1–O_1: 2.4488(2)	∠Fe_1–O_1–Fe_1: 157.086(5)	La	0.99300(6)	0.02970(1)	0.25000(1)
	b = 5.560(8) Å	2 × La_1–O_1: 2.6911(2)	∠Fe_1–O_2–Fe_1: 154.013(3)	Fe	0.00000(1)	0.50000(3)	0.00000(0)
	c = 7.843(4) Å	1 × La_1–O_2: 2.3852(3)		O1	0.71900(5)	0.30200(2)	0.02900(1)
	V = 242.34(6) Å^3	1 × La_1–O_2: 2.5774(4)		O2	0.08000(1)	0.48500(4)	0.25000(2)
	R_b = 1.64	2 × Fe_1–O_1: 1.9239(2)					
	R_f = 1.58	2 × Fe_1–O_1: 2.0862(2)					
	χ^2 = 1.12	2 × Fe_1–O_2: 2.0124(2)					
$La_{0.45}Ca_{0.55}MnO_3$ phase Orthorhombic (S.G. P*bnm*)	a = 5.447(2) Å	1 × Ca_1/La_1–O_1: 2.4541(4)	∠Mn_1–O_1–Mn_1: 161.833(3)	La	0.50600(4)	0.51900(2)	0.25000(1)
	b = 5.405(0) Å	1 × Ca_1/La_1–O_1: 2.6218(4)	∠Mn_1–O_2–Mn_1: 164.399(3)	Ca	0.50600(3)	0.51900(1)	0.25000(0)
	c = 7.618(0) Å	2 × Ca_1/La_1–O_2: 2.4792(2)		Mn	0.50000(4)	0.00000(0)	0.00000(2)
	V = 224.350(5) Å^3	2 × Ca_1/La_1–O_2: 2.6442(2)		O1	0.44410(3)	0.00000(1)	0.25000(3)
	R_b = 1.91	2 × Mn_1–O_1: 1.9288(2)		O2	0.74640(5)	0.29440(3)	0.02430(1)
	R_f = 2.72	2 × Mn_1–O_2: 1.7828(2)					
	χ^2 = 1.12	2 × Mn_1–O_2: 2.0900(2)					
LCMO–LFO @700 °C $LaFeO_3$ phase Orthorhombic (S.G. P*bnm*)	a = 5.551(0) Å	2 × La_1—O_1: 2.4475(2)	∠Fe_1–O_1–Fe_1: 157.086(5)	La	0.99300(4)	0.02970(1)	0.25000(0)
	b = 5.557(8) Å	2 × La_1–O_1: 2.6896(1)	∠Fe_1–O_2–Fe_1: 154.013(3)	Fe	0.00000(0)	0.50000(1)	0.00000(1)
	c = 7.829(9) Å	1 × La_1–O_2: 2.3849(3)		O1	0.71900(5)	0.30200(2)	0.02900(1)
	V = 242.155(5) Å^3	1 × La_1–O_2: 2.5781(4)		O2	0.08000(0)	0.48500(3)	0.25000(2)
	R_b = 2.29	2 × Fe_1–O_1: 1.9237(2)					
	R_f = 2.33	2 × Fe_1–O_1: 2.0862(2)					
	χ^2 = 1.49	2 × Fe_1–O_2: 2.0109(2)					
$La_{0.45}Ca_{0.55}MnO_3$ phase Orthorhombic (S.G. P*bnm*)	a = 5.514 (4) Å	2 × Ca_1/La_1–O_1: 2.484(2)	∠Mn_1–O_1–Mn_1: 161.739(2)	La	0.50600(2)	0.51900(3)	0.25000(1)
	b = 5.454 (9) Å	2 × Ca_1/La_1–O_1: 2.6460(2)	∠Mn_1–O_2–Mn_1: 164.429(2)	Ca	0.50600(2)	0.51900(1)	0.25000(2)
	c = 7.671 (6) Å	2 × Ca_1/La_1–O_2: 2.5013(1)		Mn	0.50000(3)	0.00000(2)	0.00000(0)
	V = 230.768(3) Å^3	2 × Ca_1/La_1–O_2: 2.6682(1)		O1	0.44410(2)	0.00000(0)	0.25000(2)
	R_b = 3.90	2 × Mn_1–O_1: 1.9420(1)		O2	0.74640(5)	0.29440(2)	0.02430(1)
	R_f = 2.45	2 × Mn_1–O_2: 1.8023(1)					
	χ^2 = 1.49	2 × Mn_1–O_2: 2.1117(1)					
LCMO–LFO @800 °C $LaFeO_3$ phase Orthorhombic (S.G. P*bnm*)	a = 5.504(0) Å	2 × La_1–O_1: 2.4310(3)	∠Fe_1–O_1–Fe_1: 157.110(6)	La	0.99300(6)	0.02970(1)	0.25000(0)
	b = 5.555(0) Å	2 × La_1–O_1: 2.6686(3)	∠Fe_1–O_2–Fe_1: 154.018(5)	Fe	0.00000(1)	0.50000(2)	0.00000(2)
	c = 7.770(0) Å	1 × La_1–O_2: 2.3633(5)		O1	0.71900(5)	0.30200(3)	0.02900(1)
	V = 237.584(7) Å^3	1 × La_1–O_2: 2.5743(4)		O2	0.08000(0)	0.48500(4)	0.25000(3)
	R_b = 3.00	2 × Fe_1–O_1: 1.9112(3)					
	R_f = 3.27	2 × Fe_1–O_1: 2.0780(2)					

Table 1 (*continued*)

Composition and phase	Lattice parameters	Bond distance (Å)	Bond angle (°)	Atomic coordinates			
				Atom	x	y	z
	χ^2 = 1.75	2 × Fe_1–O_2: 1.9937(3)					
$La_{0.45}Ca_{0.55}MnO_3$ phase Orthorhombic (S.G. P*bnm*)	a = 5.487(8) Å	1 × Ca_1/La_1–O_1: 2.4721(3)	∠Mn_1–O_1–Mn_1: 161.987(3)	La	0.50600(3)	0.51900(5)	0.25000(2)
	b = 5.489(1) Å	1 × Ca_1/La_1–O_1: 2.4721(9)	∠Mn_1–O_2–Mn_1: 164.361(7)	Ca	0.50600(3)	0.51900(4)	0.25000(1)
	c = 7.7410(0) Å	2 × Ca_1/La_1–O_2: 2.5126(4)		Mn	0.50000(2)	0.00000(1)	0.00000(2)
	V = 233.200(4) Å^3	2 × Ca_1/La_1–O_2: 2.6801(4)		O1	0.44410(3)	0.00000(1)	0.25000(3)
	R_b = 1.82	2 × Mn_1–O_1: 1.9592(2)		O2	0.74640(6)	0.29440(3)	0.02430(0)
	R_f = 2.14	2 × Mn_1–O_2: 1.8018(5)					
	χ^2 = 1.75	2 × Mn_1–O_2: 2.1153(2)					
LCMO–LFO @1000 °C $La_{0.725}Ca_{0.275}Mn_{0.5}Fe_{0.5}O_3$: (100%) Orthorhombic (S.G. P*bnm*)	a = 5.494(0) Å	1 × Ca_1/La_1–O_1: 2.4752(3)	∠Mn_1/Fe_1–O_1–Mn_1/Fe_1: 161.971(2)	La	0.50600(4)	0.51900(4)	0.25000(1)
	b = 5.478(0) Å	1 × Ca_1/La_1–O_1: 2.6571(2)	∠Mn_1/Fe_1–O_2–Mn_1/Fe_1: 164.356(2)	Ca	0.50600(3)	0.51900(2)	0.25000(2)
	c = 7.744(0) Å	2 × Ca_1/La_1–O_2: 2.5127(1)		Mn	0.50000(1)	0.00000(0)	0.00000(2)
	V = 233.100(4) Å^3	2 × Ca_1/La_1–O_2: 2.6799(1)		O1	0.44410(2)	0.00000(1)	0.25000(0)
	R_b = 3.15	2 × Mn_1/Fe_1–O_1: 1.9602(2)		O2	0.74640(3)	0.29440(2)	0.02430(0)
	R_f = 4.63	2 × Mn_1/Fe_1–O_2: 1.8015(1)					
	χ^2 = 1.26	2 × Mn_1/Fe_1–O_2: 2.1139(1)					

La 3d, Ca 2p, Mn 2p, Fe 2p and O 1s regions were collected. The XPS spectra were fitted using MultiPak Spectrum: ESCA. The Shirley method was used to subtract the spectral background. The dc-magnetization measurements were carried out using a vibrating sample magnetometer attached to the physical property measurement system, Quantum Design Inc., (USA). The dc magnetic measurements were performed on the compact powder sample inside the Teflon capsule. The magnetic data were recorded as a function of temperature and applied magnetic field of ±9 Tesla at fixed temperatures.

Results

Structure and microstructure

Fig. 1 shows the powder X-ray diffraction patterns of the parent phases $LaFeO_3$ (LFO), $La_{0.45}Ca_{0.55}MnO_3$ (LCMO) and their 1 : 1 composite $La_{0.45}Ca_{0.55}MnO_3$–$LaFeO_3$ (LCMO–LFO) annealed at different temperatures, namely at 600, 700, 800 and 1000 °C. The patterns of LFO and LCMO synthesized at 500 °C can be well indexed with *Pbnm* space group without any additional reflection confirming the purity of the parent phases (Fig. 1(a) and (b)). The pattern of the LCMO–LFO composite annealed at 600 °C clearly attests the appearance of both phases, and it can be indexed with combined phases (Fig. 1(c)). However, with the increase in annealing temperature, the identity of the parent phases was gradually suppressed, resulting to the formation of a single phase $La_{0.725}Ca_{0.275}Mn_{0.5}Fe_{0.5}O_3$ (Fig. 1(f)). This is clearly evidenced from the enlarged view of the main peaks in the insets of Fig. 1(c)–(e). The evolution of PXRD patterns with annealing temperature supports the formation of the product phase out of the parent phases at the interfaces of the composite grains. The persistence of parent phases was realized up to the annealing temperature of 800 °C (Fig. 1(e)). The refinement parameters and cell constants for all of the samples are summarized in Table 1. It is worth noting that the diffraction peak position of LCMO shifted towards high angle for the 700 and 800 °C annealed samples, which are clear from the enlarged plot between 31–34° (Fig. 1(d) and (e)). This is also reflected in the cell parameters given in Table 1. The cell volume of the LCMO phase increased from 224.350(5) Å^3 for the 600 °C annealed sample to 230.768(3) Å^3 for the 700 °C sample. Actually, at this point, there should be a coexistence of three phases: LCMO, LFO and the phase formed at the interface. This may be at the origin of the peak broadening in the diffraction patterns for the 700 and 800 °C annealed samples. However, we have continued to refine the patterns with the LCMO and LFO phases only. Up to 800 °C, the LFO phase retains its identity (Fig. 1(e)). For the 1000 °C sample, it results in a single sharp peak, confirming a homogeneous phase formation. This observation is highly consistent with the observed magnetic behaviour discussed in the following section.

The FE-SEM micrographs of nanocrystalline $La_{0.45}Ca_{0.55}MnO_3$ and $LaFeO_3$, as well as for the composite, are shown in supplementary Fig. S1 (ESI†). The particle size of LCMO is rather small compared to that of the LFO (Fig. S1(a) and (b), ESI†). The temperature evolution of the particle size of the composite revealed the increase in particle size with the temperature, as expected. The cationic ratio obtained from EDX analysis for the parent phases matches well with the nominal cationic composition (Fig. S2 and S3, ESI†). More importantly, the gradual progress of the interface reaction is adequately probed from elemental mapping. A comparison of the elemental mapping for the LCMO–LFO composite annealed at 700 °C and 1000 °C is shown in Fig. 2. Fig. 2(a) clearly reveal the appearance of LCMO and LFO grains.

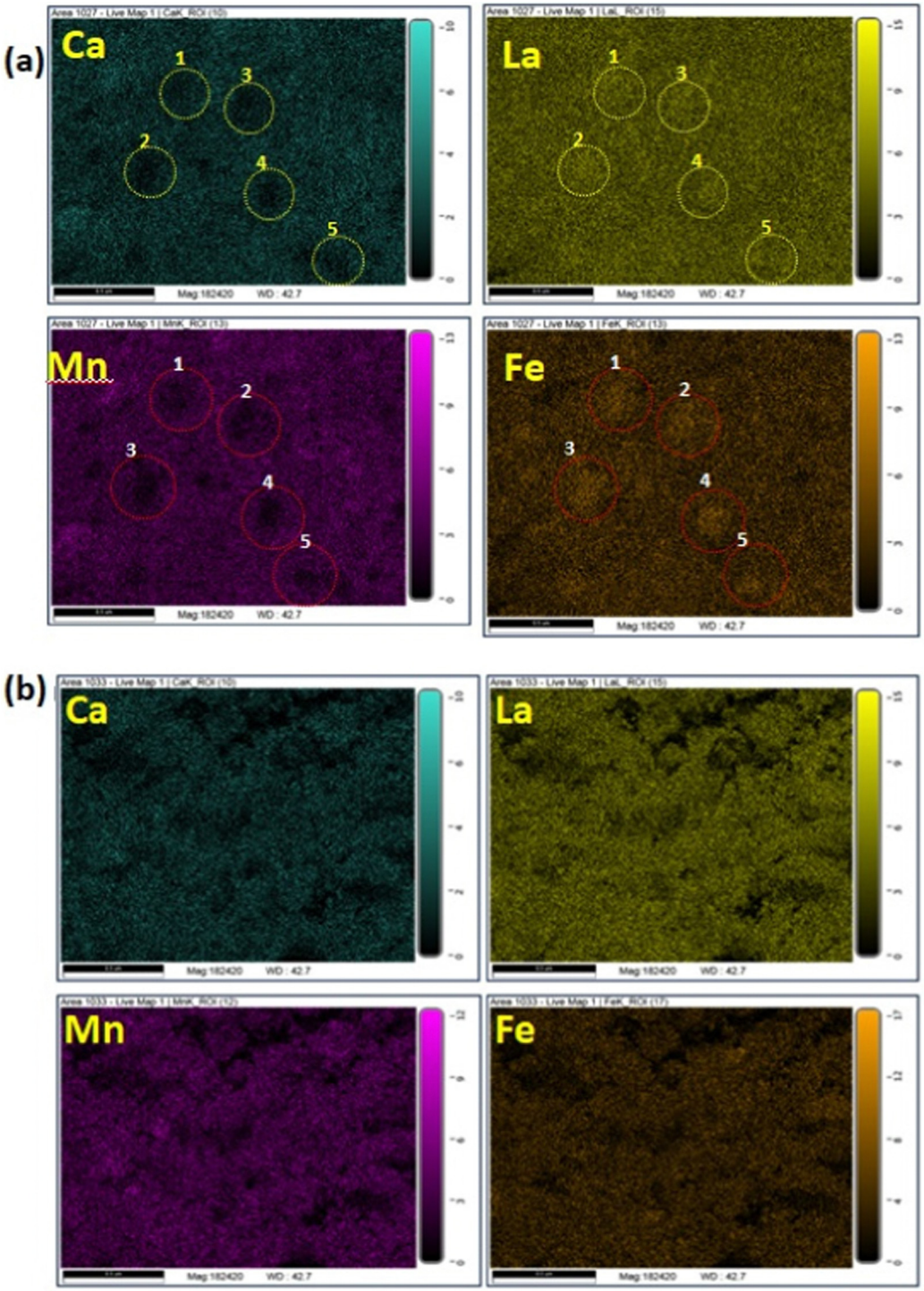

Fig. 2 The elemental mapping of the $La_{0.45}Ca_{0.55}MnO_3$–$LaFeO_3$ (LCMO–LFO) composite annealed at: (a) 700 °C and (b) 1000 °C.

The Ca-depleted encircled regions (numerically marked) in the Ca panel is complemented by brighter spots in the La panel with corresponding numeric values. These brighter spots in the La panel indicated the LFO grains. This is substantiated by the appearance of the Mn-depleted region at the same positions in the Mn panel and the brighter spots in the Fe panel, as shown by the numerically encircled zones. Similar features in the elemental mapping are noticed for the 600 °C and 800 °C samples (Fig. S4 and S6, ESI†). The separated grain-type features of LCMO and LFO are completely suppressed in the 1000 °C annealed samples, resulting in a homogeneous distribution of each element present in the samples, as shown in Fig. 2(b). This is further evidenced from the EDX analysis of the 1000 °C annealed samples corresponding to the composition $La_{0.725}Ca_{0.275}Mn_{0.5}Fe_{0.5}O_3$ (Fig. S7,

ESI†). However, the EDX elemental ratios of the 600, 700 and 800 °C annealed samples show variable ratios depending on the probed area (Fig. S4–S6, ESI†). This observation suggests the progressive reaction at the interfaces of LCMO and LFO to produce the new perovskite of average composition. However, the separate diffraction peaks of the new phase are not observed, which may possibly be due to very similar cell parameters. The product phase developed at the interface at lower temperatures is likely to have Mn and Fe ordering, and it gets randomized at higher temperature. A schematic diagram of the inter-growth phase formation at the interface of the pristine phases with cation ordering is shown in Fig. S8 (ESI†). A significant fraction of the product interface phase with Mn and Fe ordering is expected to show dominating properties.

TEM analysis

In order to substantiate our proposed model of the interfacial phase formation, as shown in Fig. S8 (ESI†), we have carried out TEM, EDX, ED and HAADF-STEM along the main zone axes of the cubic structure: [010] and [110]. We have shown the EDX-STEM elemental mapping of all three samples sintered at 700, 800 & 1000 °C in Fig. 3. The EDX mapping panels in Fig. 3(a) and (b) for the 700 °C and 800 °C annealed composites, respectively, clearly reveal the coexistence of pristine phases, along with the product phases formed in the forms of thin lamellas at the interfaces. However, it is clearly visualized from the lower panel in Fig. 3(c) that all of the elements are practically homogeneously distributed, unlike the contrasting features existing in Fig. 3(a) and (b) for the 700 °C & 800 °C annealed composites. These results are in corroboration with the FE-SEM analysis presented in the preceding section. This supported our proposed model, and this is further strengthened from the magnetic measurements. We have further carried out high-resolution HAADF-STEM along the [010] and [110] directions together with ED and simultaneously acquired EDX-STEM elemental mapping for the 800 °C annealed sample for a specific crystallite (Fig. 4a and b). The ED shows the well crystalline feature of the sample with a typical perovskite cell parameter. The EDX-STEM mapping along with the Fe/Mn elemental line scan profile across the Fe/Mn lamella over 20 nm for the 800 °C annealed sample is shown on the right panel of Fig. 4(a). It nicely depicts the Fe-rich region at the center of the crystallite and the existence of a comparable amount of Fe and Mn on both sides of the Fe-dominant region. This further authenticates our model. However, our high-resolution HAADF-STEM images do not directly support the chess-board type ordering of Mn ($Z = 25$) and Fe ($Z = 26$) due to their adjacent positions in the periodic table. In contrast, the indirect evidence of ordering is supported from the magnetization data discussed in the following section. It is worthwhile to mention that ED is also unable to detect the same results due to the structural identity of all of the pristine and intergrowth phases. The corresponding low-magnification and high-resolution HAADF-STEM image along the [110] direction, ED pattern and EDX-STEM elemental mapping are taken from the same crystallite shown in the lower panel in Fig. 4(b).

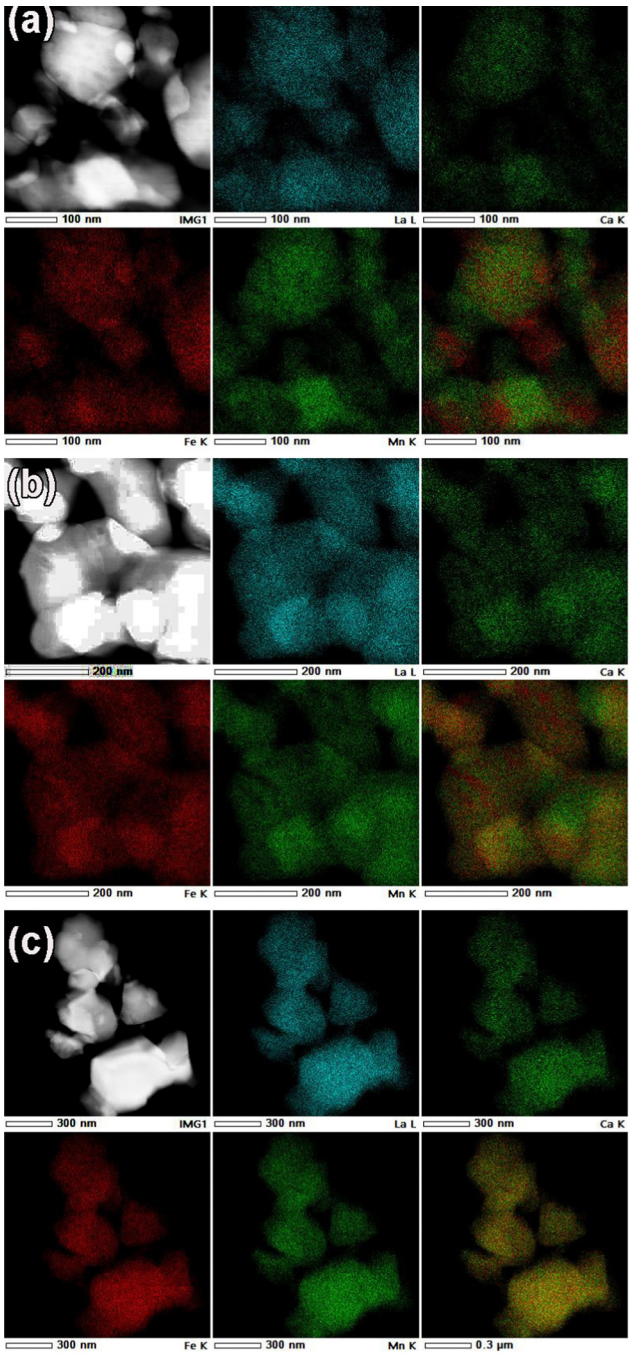

Fig. 3 Low magnification HAADF-STEM image and simultaneously acquired EDX-STEM elemental mapping of La L, Ca K, Fe K, Mn K, Fe and Mn overlayed color images for samples annealed at (a) 700 °C, (b) 800 °C, (c) 1000 °C.

XPS study

The XPS analysis was carried out to obtain a clear understanding of the oxidation states and elemental compositions present in all of the developed samples. All of the peaks were calibrated with respect to the C 1s peak positioned at 284.6 eV. The wide-scan XPS spectra of all of the samples are depicted in Fig. 5, which clearly reveal that there are no foreign elements present

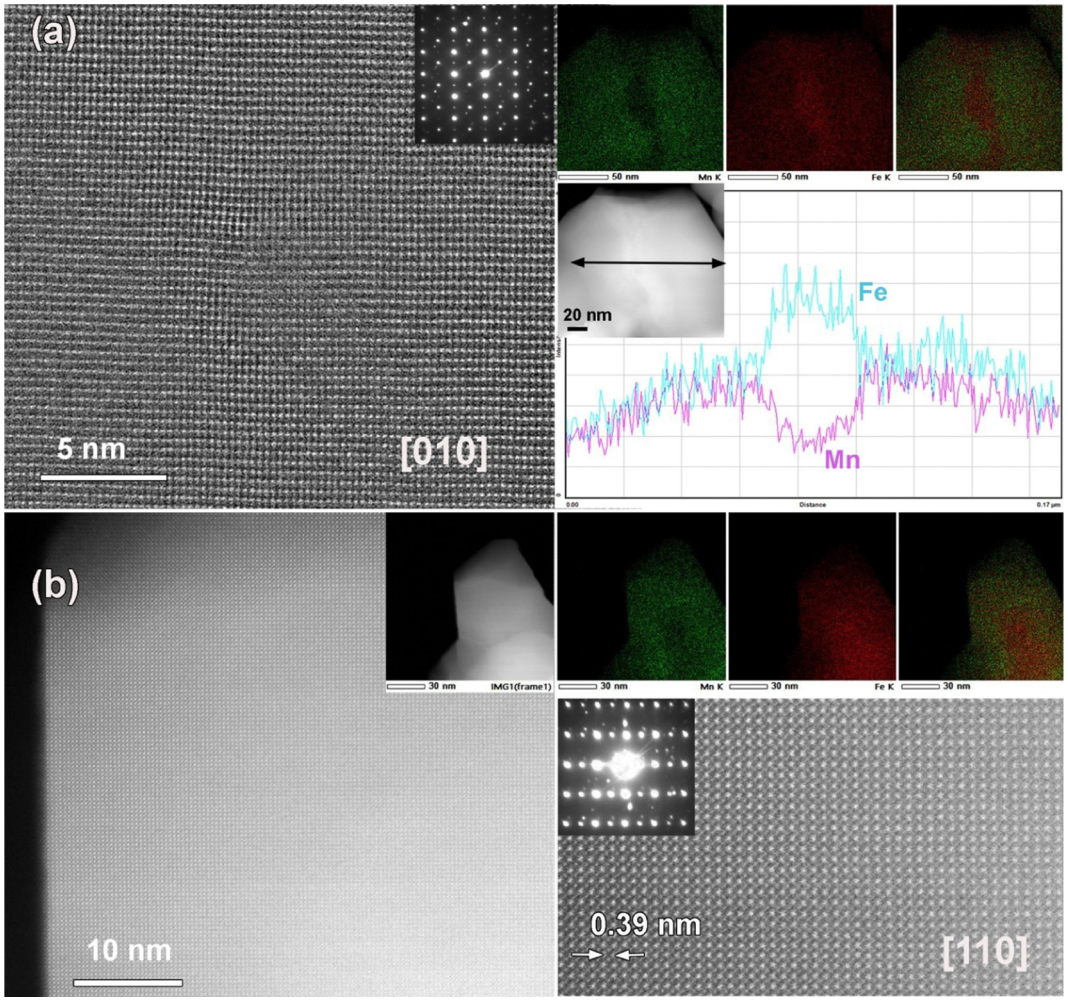

Fig. 4 (a) Left panel – [010] high-resolution HAADF-STEM image and corresponding ED pattern taken from the region depicted in the low-magnification image at the right panel. EDX-STEM elemental mapping of Mn K, Fe K and the overlayed color image for the same region is present in the right panel. Elemental quantitative line scan profile for Fe and Mn is in the right bottom panel. (b) Corresponding low-magnification and high-resolution [110] HAADF-STEM image, ED pattern and EDX-STEM elemental mapping taken from the same crystal area.

on the surfaces of the material. In order to determine the oxidation state of the composition, the high-resolution scans of the La 3d, Fe 2p and O 1s spectra of the $LaFeO_3$ (LFO) sample were analysed and are shown in Fig. 6. Similar to this, Fig. 7 shows the high-resolution scans of the La 3d, Ca 2p, Mn 2p, and O 1s spectra of $La_{0.45}Ca_{0.55}MnO_3$ (LCMO). Similarly, the high-resolution scans of the La 3d, Ca 2p, Mn 2p, Fe 2p and O 1s spectra of LCMO–LFO annealed at 600 °C & 1000 °C were analysed, and are shown in Fig. 8 and 9. The high-resolution scans of all of the elements present in all of the samples were deconvoluted. A detailed analysis of different elemental compositions, along with the deconvoluted peaks corresponding to the different B.E.'s, are summarised in Table 2.

The slow scan of the La 3d spectra in all of the samples showed a broad peak that is deconvoluted into three additional peaks, indicating the presence of La^{3+}, satellite peaks[61] and La_2O_3 or $La(OH)_3$,[62] respectively. The presence of La_2O_3 or $La(OH)_3$ can be due to the chemisorption of oxygen and moisture with the chemically active La element. It is very difficult to predict the contributions of each La_2O_3 and $La(OH)_3$ separately, so the peaks located at 838–839.50 eV ($3d_{5/2}$) and 862.00–864.65 eV ($3d_{3/2}$) correspond to the mixed composition of La_2O_3 and $La(OH)_3$, respectively. It is clearly evident that the change in the elemental composition, temperature and intimate mixing of the samples did not affect the composition of the La^{3+} ions. The deconvolution of the slow scan of the Ca 2p spectra showed the presence of Ca^{2+} ions, and CaO, $CaCO_3$ or $Ca(OH)_2$ species in the $La_{0.45}Ca_{0.55}MnO_3$ (LCMO), $(LCMO)_{0.5}(LFO)_{0.5}$ samples annealed at 600 °C & 1000 °C. The presence of CaO, $CaCO_3$ or $Ca(OH)_2$ can be due to the interaction of oxygen, carbon dioxide and moisture content present in the atmosphere with the chemically active Ca^{2+} ions, leading to the formation of the former chemisorbed species on the surface of the material.[63] It is very difficult to decide the B.E. corresponding to each CaO, $CaCO_3$ or $Ca(OH)_2$ species, so the undesired compound chemisorbed on the samples may be a mixture of all three.

The deconvoluted peaks of the slow scan of Fe 2p in $LaFeO_3$ (LFO), of $(LCMO)_{0.5}(LFO)_{0.5}$ annealed at 600 °C and 1000 °C

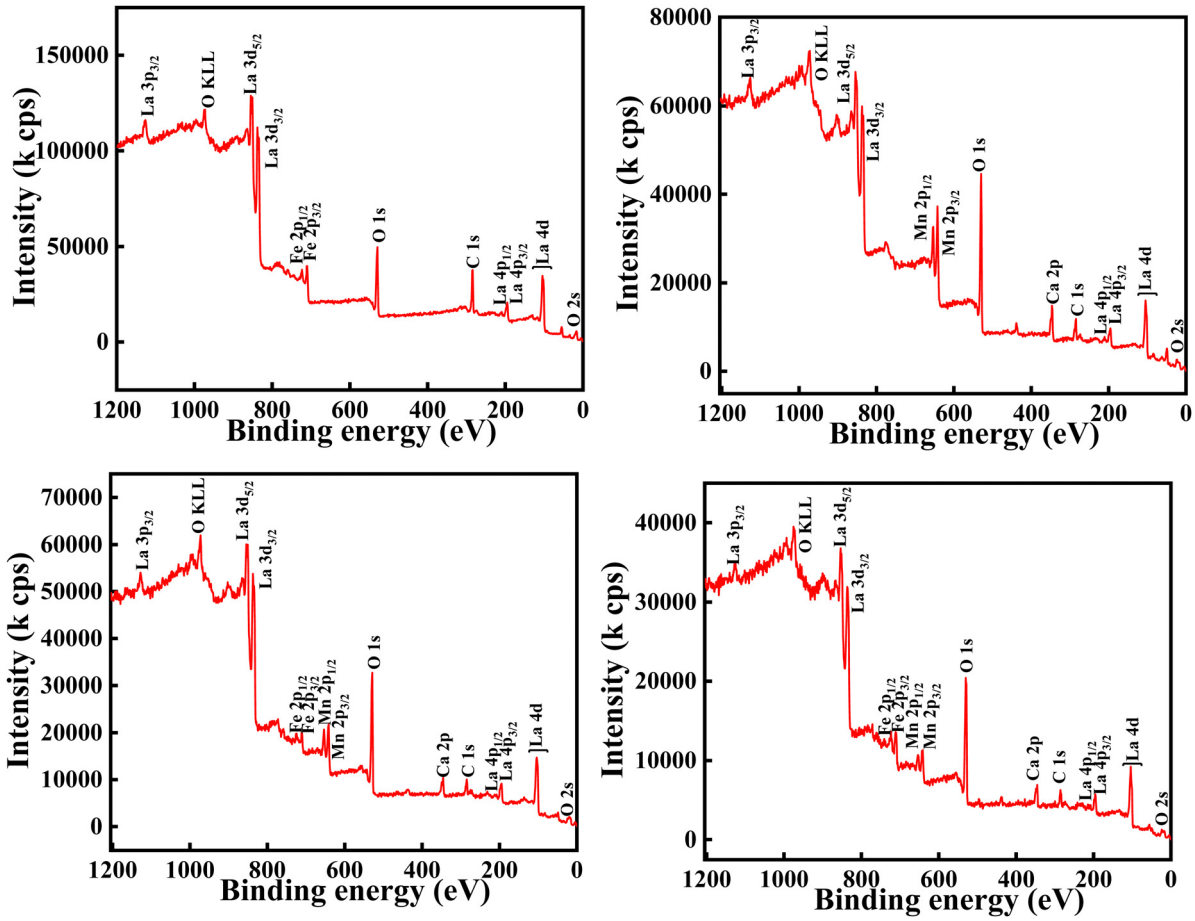

Fig. 5 Wide XPS spectra of $LaFeO_3$ (LFO) (top panel, left), $La_{0.45}Ca_{0.55}MnO_3$ (LCMO) (top panel, right), LCMO–LFO annealed at 600 °C (lower panel, left) and LCMO–LFO annealed at 1000 °C (lower panel right).

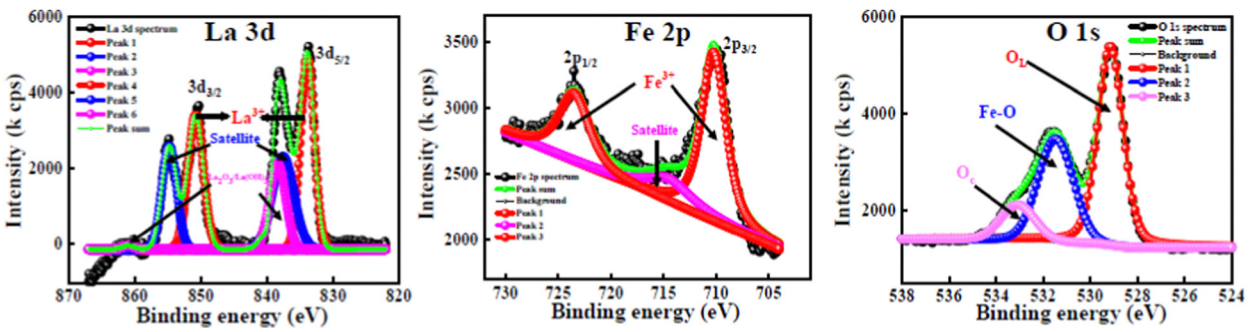

Fig. 6 High-resolution XPS spectra of La 3d, Fe 2p and O 1s for $LaFeO_3$ (LFO).

samples, indicated the presence of Fe in +3 oxidation state only.[64] However, in the $LaFeO_3$ (LFO) sample, the B-site is fully occupied by Fe^{3+} ions. In the $(LCMO)_{0.5}(LFO)_{0.5}$ sample annealed at 600 °C and 1000 °C, Fe^{3+} is occupying 50% of B site. The deconvolution of the slow scan of the Mn 2p spectra in the $(LCMO)_{0.5}(LFO)_{0.5}$ samples annealed at 600 °C & 1000 °C showed the presence of mixed oxidation states of the Mn metal, *i.e.*, Mn^{3+} and Mn^{4+} ions.[65] It was clearly observed that there is a greater presence of Mn^{4+} ions than Mn^{3+} ions in the three samples (reflected in Table 2). However, the percentage of Mn^{3+} and Mn^{4+} ions occupying the B-site was calculated using the peak area done by XPS peak fit software, which is around 44.82 and 55.18, 22.48 and 27.52, 22.93 and 27.07 in the LCMO, $(LCMO)_{0.5}(LFO)_{0.5}$ annealed at 600 °C and $(LCMO)_{0.5}(LFO)_{0.5}$ annealed at 1000 °C. Moreover, the percentage of occupancy of Mn ions in $(LCMO)_{0.5}(LFO)_{0.5}$ annealed at 600 °C and 1000 °C is calculated based on the peak area, which pertains to the Mn 2p spectra only, so the total percentage will be 100. However, the B site is partially occupied by Fe^{3+} ions in $(LCMO)_{0.5}(LFO)_{0.5}$ annealed at 600 °C and 1000 °C. Therefore, the percentage of

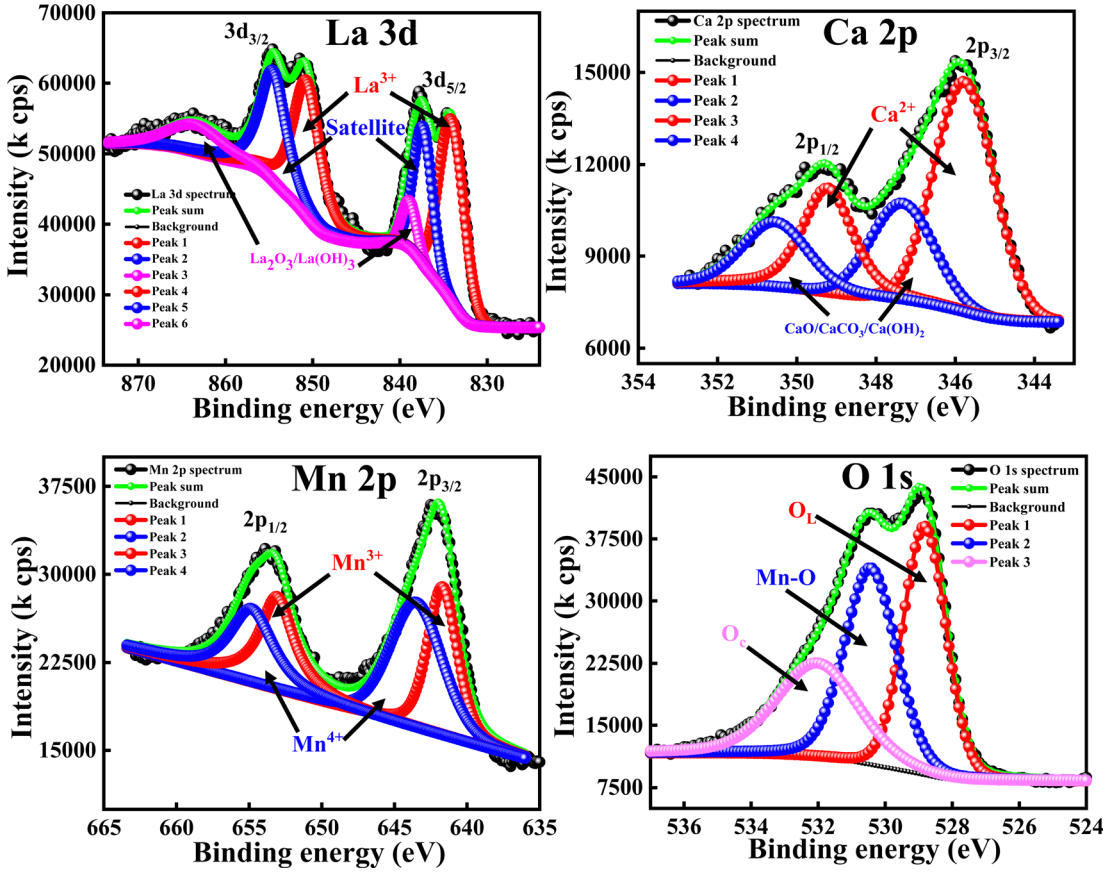

Fig. 7 High-resolution XPS spectra of La 3d, Ca 2p, Mn 2p and O 1s for $La_{0.45}Ca_{0.55}MnO_3$ (LCMO).

occupancy of Mn ions in the B site will be 50%. The resulting percentage of occupancy of Mn ions in the B site matches with the stoichiometric composition of the three samples. Similarly, the high-resolution O 1s spectra of all samples showed a broad peak and they are deconvoluted into three subpeaks, corresponding to the lattice oxygen (O_L) having the lowest B.Es, M–O bond (M = Mn/Fe) having the middle B.Es, and chemisorbed oxygen (O_c) having the highest B.Es.[61,66] The crucial observation from the XPS analysis is that the percentage of occupancy of La^{3+} ions in the A-site, Fe^{3+}, Mn^{3+} and Mn^{4+} ions in the B-site is exactly matching with the stoichiometric composition/ratio of the samples. Moreover, the mixed occupancy of Mn and Fe in B-site is likely to influence the magnetic properties of nanocomposite perovskite materials.

Magnetic properties

Fig. 10 shows the temperature-dependent magnetization of LFO, LCMO and their composites annealed at different temperatures under an applied magnetic field of 100 Oe. The observed magnetic property of LFO nanoparticles is shown in Fig. 10(a). This is in good agreement with the reported magnetization of $LaFeO_3$ nanoparticles.[67] There is a large thermomagnetic irreversibility between the ZFC-FC data. This could be due to the random freezing of the magnetic moment cooled under zero applied field, or there can be magnetic frustration in the system due to competing magnetic interaction. The isothermal magnetization measurements shown in Fig. 11(a) suggest the ferromagnetic feature of LFO nanoparticles. LFO is an antiferromagnetic material with a slight spin canting, which is responsible for the weak ferromagnetic behavior.[68,69] In addition to the canted internal spin, another possible source of the ferromagnetic component is the uncompensated disordered surface spins arising out of the relaxed superexchange interaction.[70–72] The bulk $La_{0.45}Ca_{0.55}MnO_3$ is a typical charge ordered system with the charge ordering temperature (T_{CO}) at 220 K.[73,74] However, with the decrease in particle size in nanodomains for manganite, the T_{CO} decreases and is eventually suppressed below a critical size.[75] In the present work, the ZFC data of $La_{0.45}Ca_{0.55}MnO_3$ show a broad hump around 130 K, whereas the FC data continue to increase below 250 K (Fig. 10(b)). The ZFC-FC data show bifurcation below 200 K, which may be related to the magnetic inhomogeneity of the system. There is a jump in magnetization near zero applied field with a slight opening of the loop, but it lacks the saturation even at 9 Tesla (Fig. 11(b)), suggesting the coexistence of ferromagnetic and antiferromagnetic phases. The LCMO–LFO composite annealed at 600 °C shows a very similar feature as the pristine LCMO phase (Fig. 10(c)). The $M(H)$ curves for

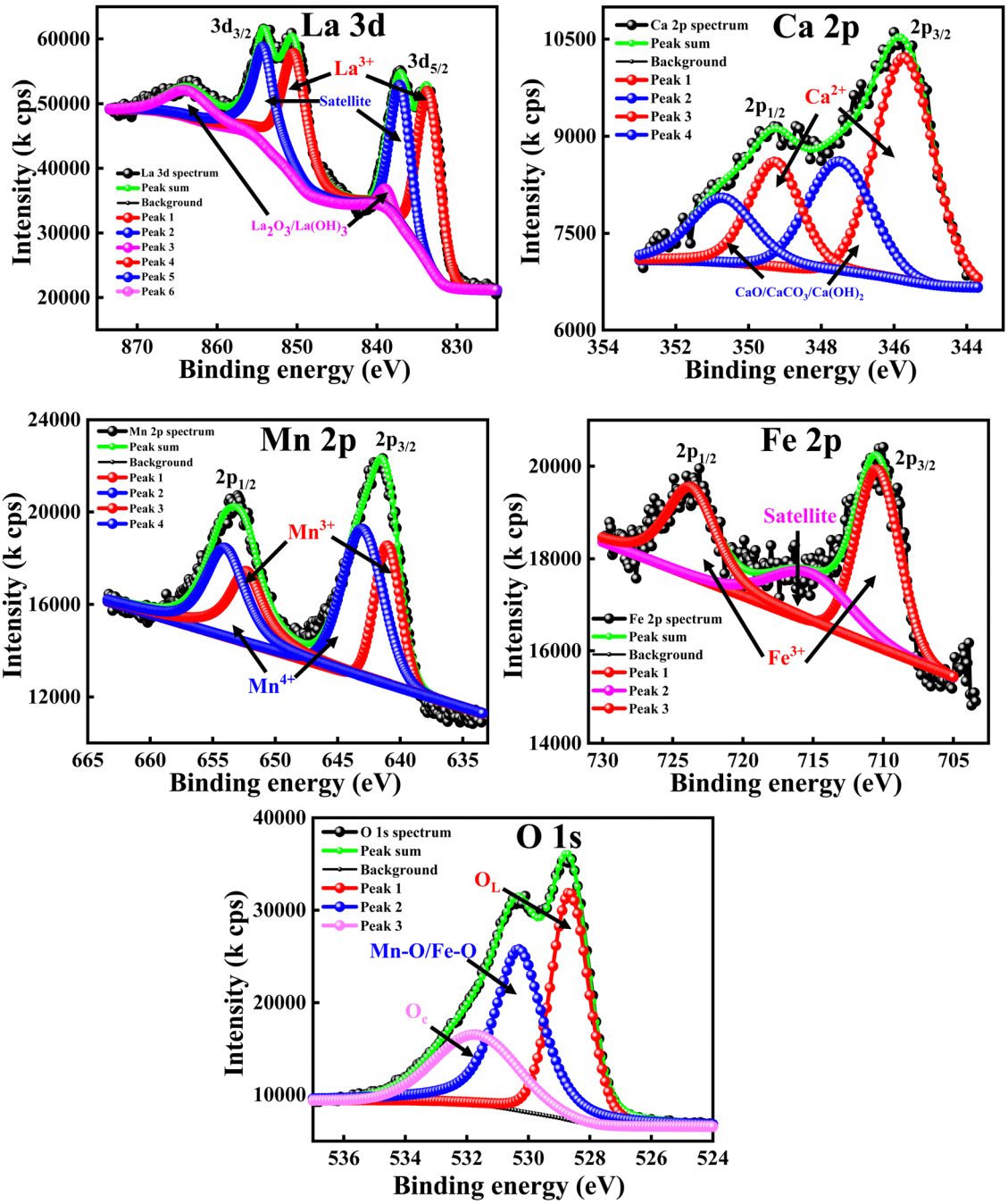

Fig. 8 High-resolution XPS spectra of La 3d, Ca 2p, Mn 2p, Fe 2p and O 1s for LCMO–LFO annealed at 600 °C.

LCMO and LCMO–LFO annealed at 600 °C show similar types of behavior (Fig. 11(b)&(c)). The temperature derivative (dM/dT) plots of both the LCMO and LCMO–LFO annealed at 600 °C exhibit broad minima centered around 200 K, suggesting the onset temperature (Fig. 12(a) and (b)). These indicate the dominating magnetic behavior of $La_{0.45}Ca_{0.55}MnO_3$ in the composite phase annealed at lower temperature. This also is clear from the high value of magnetization of LCMO compared to LFO. However, a significant change in magnetization is noticed for the 700 and 800 °C annealed samples (Fig. 10(d) and (e)). This is consistent with the observation of the change in the PXRD pattern in Fig. 1(d) and (e), as discussed in the preceding section. The magnetization value decreases, but the transition temperature shifted upwards by about 25 K, which is clearly observed from the dM/dT curves shown in Fig. 12(d) and (e). The $M(H)$ curves indicate the occurrence of ferromagnetic and antiferromagnetic phases (Fig. 11(d) and (e)). These upward shifts in the ordering temperature can be attributed to the development of new phases across the interfaces of LCMO and LFO, where a possible ordering of Mn and Fe takes

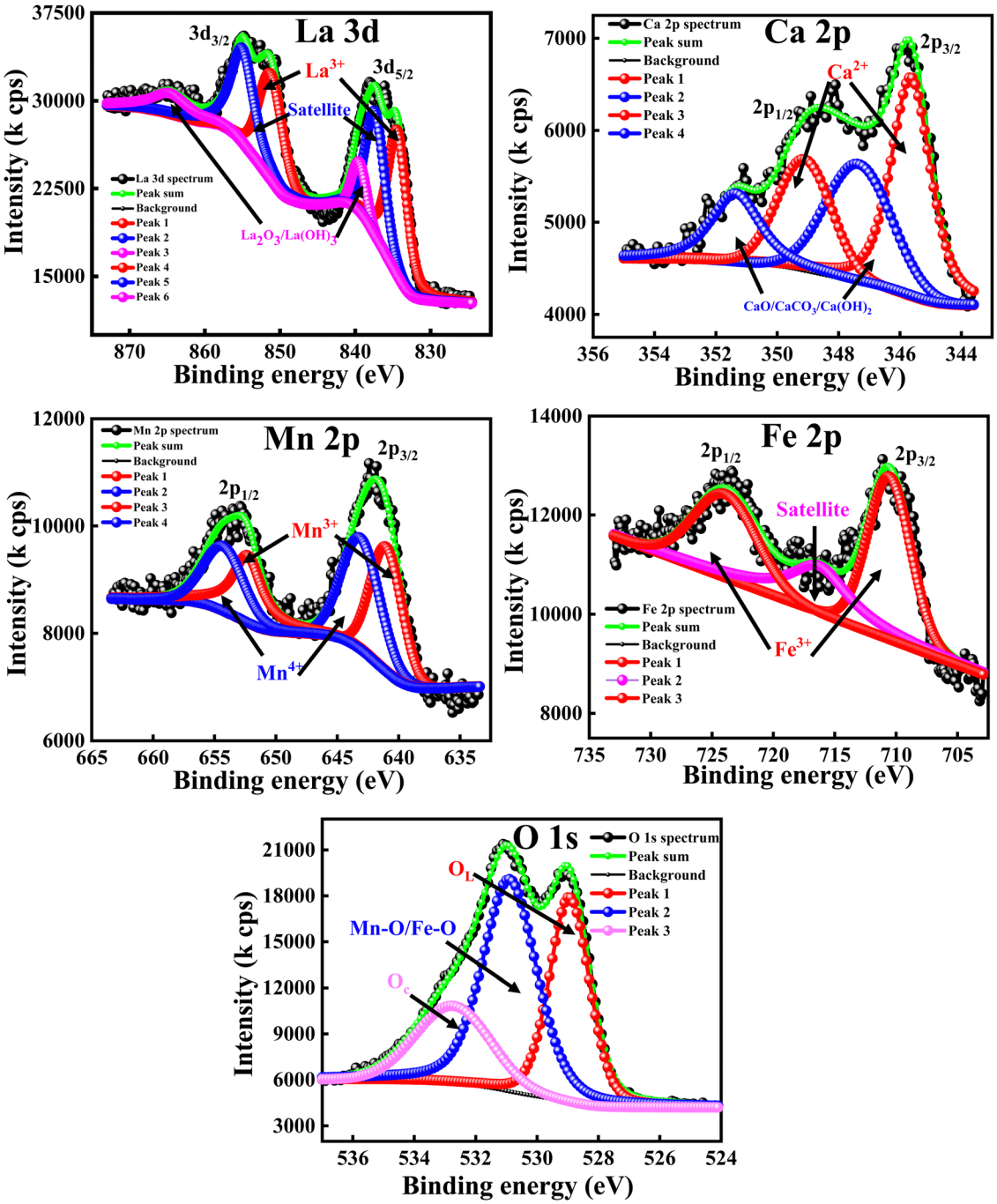

Fig. 9 High-resolution XPS spectra of La 3d, Ca 2p, Mn 2p, Fe 2p and O 1s for LCMO–LFO annealed at 1000 °C.

place, which is discussed below. On further increase in the annealing temperature to 1000 °C, no long-range ordering at high temperature is apparent (Fig. 10(f)). This is also indicated from the dM/dT plot, as shown in Fig. 12(f). This can be ascribed to the complete randomization of Mn and Fe in the interfacial product phase of $La_{0.725}Ca_{0.275}Mn_{0.5}Fe_{0.5}O_3$. This is consistent with the homogeneous distribution of Mn and Fe observed in elemental mapping (Fig. 2(b)). This result is very much consistent with the reported results for $La_{1-x}A_xFe_{0.5}Mn_{0.5}O_3$ perovskites.[57,58] However, an opening in the hysteresis loop and reduction in magnetization are observed at 3 K, which suggests that there are residual ferromagnetic droplets in the system (Fig. 11(f)). These results suggest that by controlling the annealing temperature, a possible ordering of Mn and Fe in the interface reaction product of LCMO and LFO can be achieved. Such ordering of Mn and Fe was reported in a 1 : 1 ratio of the $LaMnO_3$ and $LaFeO_3$ superlattices, but not in the bulk sample.

Now, we will discuss the possibility of Mn and Fe ordering across the LCMO–LFO interfaces to understand the observed magnetic behaviour for the 700 and 800 °C annealed samples.

Table 2 Summary of the XPS analysis on different elemental compositions present in $LaFeO_3$ (LFO), $La_{0.45}Ca_{0.55}MnO_3$ (LCMO), and LCMO–LFO composites annealed at 600 °C and 1000 °C

	La 3d spectrum		Mn 2p spectrum		O 1s spectrum	
Composition	B.E. (eV)	Area (%)	B.E. (eV)	Area (%)	B.E. (eV)	Area (%)
$LaFeO_3$(LFO)	834.12 ($3d_{5/2}$, La^{3+})	27.11			529.14 (O_L)	54.41
	837.55 (satellite)	20.91			531.45 (Fe–O)	34.31
	838.10 (La_2O_3/$La(OH)_3$)	14.14			533.07 (O_c)	11.28
	850.88 ($3d_{3/2}$, La^{3+})	21.56				
	854.70 (satellite)	15.66				
	862.00 (La_2O_3/$La(OH)_3$)	0.62				
$La_{0.45}Ca_{0.55}MnO_3$ (LCMO)	834.48 ($3d_{5/2}$, La^{3+})	26.49	641.68 ($2p_{3/2}$, Mn^{3+})	24.53	528.82 (O_L)	38.15
	837.50 (satellite)	14.14	643.84 ($2p_{3/2}$, Mn^{4+})	33.33	530.82 (Mn/Fe)–O	34.12
	839.20 (La_2O_3/$La(OH)_3$)	3.31	653.05 ($2p_{1/2}$, Mn^{3+})	20.29	532.01 (O_c)	27.73
	851.20 ($3d_{3/2}$, La^{3+})	25.83	654.64 ($2p_{1/2}$, Mn^{4+})	21.85		
	854.44 (satellite)	21.09				
	863.58 (La_2O_3/$La(OH)_3$)	9.14				
LCMO–LFO@600 °C	833.56 ($3d_{5/2}$, La^{3+})	25.36	641.22 ($2p_{3/2}$, Mn^{3+})	22.92	528.68 (O_L)	41.44
	837.06 (satellite)	18.75	643.59 ($2p_{3/2}$, Mn^{4+})	31.96	530.33 (Mn/Fe)–O	34.07
	838.92 (La_2O_3/$La(OH)_3$)	1.44	652.48 ($2p_{1/2}$, Mn^{3+})	22.04	531.70 (O_c)	24.49
	850.32 ($3d_{3/2}$, La^{3+})	26.90	654.24 ($2p_{1/2}$, Mn^{4+})	23.08		
	854.12 (satellite)	19.65				
	863.45 (La_2O_3/$La(OH)_3$)	7.90				
LCMO–LFO@1000 °C	834.42 ($3d_{5/2}$, La^{3+})	25.16	641.20 ($2p_{3/2}$, Mn^{3+})	27.86	528.94 (O_L)	38.40
	837.37 (satellite)	19.69	643.59 ($2p_{3/2}$, Mn^{4+})	31.19	530.89 (Mn/Fe)–O	41.24
	839.48 (La_2O_3/$La(OH)_3$)	5.16	652.32 ($2p_{1/2}$, Mn^{3+})	18.00	532.73 (O_c)	20.36
	851.20 ($3d_{3/2}$, La^{3+})	22.40	654.57 ($2p_{1/2}$, Mn^{4+})	22.95		
	854.98 (satellite)	19.25				
	864.65 (La_2O_3/$La(OH)_3$)	8.34				

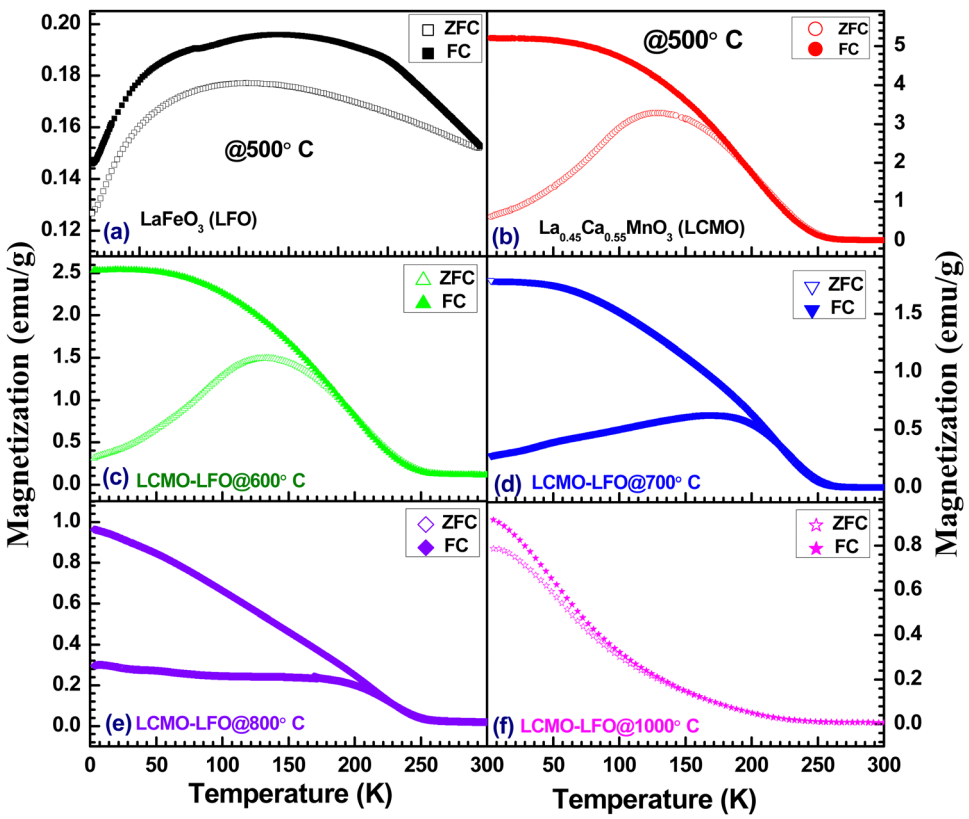

Fig. 10 Temperature-dependent magnetization of (a) $LaFeO_3$ (LFO), (b) $La_{0.45}Ca_{0.55}MnO_3$ (LCMO) and LCMO–LFO composite annealed at: (c) 600 °C, (d) 700 °C, (e) 800 °C and (f) 1000 °C, measured under an applied magnetic field of 100 Oe.

The suppression of charge ordering with the evolution of the ferromagnetic phase upon the reduction in the particle size is reported for several manganite systems including (La,Ca)–Mn–O.[75–78] On the other hand, the T_{CO} increases with the increase

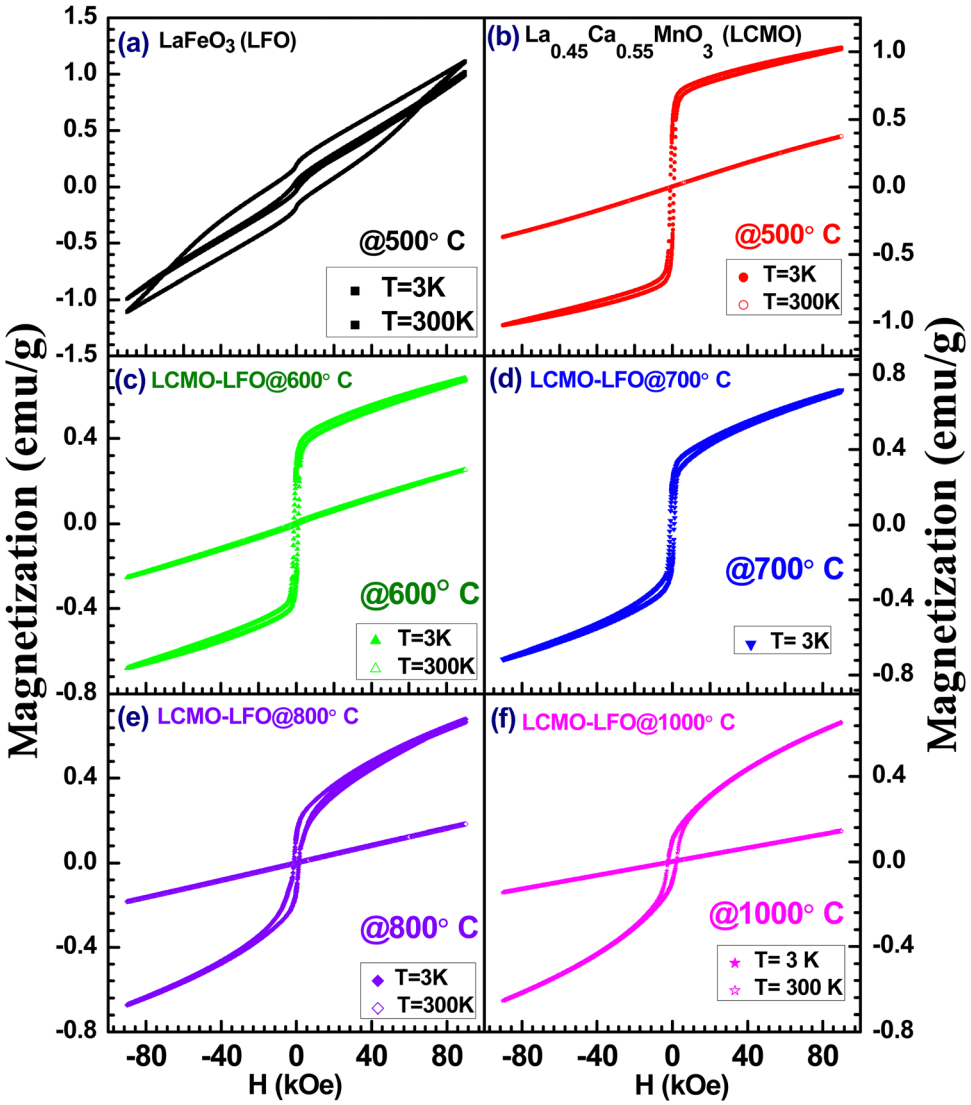

Fig. 11 Field-dependent isothermal magnetization of (a) $LaFeO_3$ (LFO), (b) $La_{0.45}Ca_{0.55}MnO_3$ (LCMO) and LCMO–LFO composite annealed at: (c) 600 °C, (d) 700 °C, (e) 800 °C and (f) 1000 °C.

in particle size.[75] It is reported that the $La_{0.45}Ca_{0.55}MnO_3$ nanoparticle shows T_{CO} at 235 K, and bulk synthesized at 1400 °C exhibits T_{CO} at 250 K.[79] It should also be noted that the T_{CO} steeply changed with a Ca-concentration above 0.5 in $La_{1-x}Ca_xMnO_3$.[80] Thus, a slight change in stoichiometry may abruptly change the ordering temperature. The phase diagram of $La_{1-x}Ca_xMnO_3$ revealed that the T_{CO} for the bulk $La_{0.45}Ca_{0.55}MnO_3$ composition is 220 K.[74,80] The observed magnetic transition in the $La_{0.45}Ca_{0.55}MnO_3$–$LaFeO_3$ composite derived from the minima in the dM/dT plots for the 700 and 800 °C annealed samples is 225 K (Fig. 12(c) and (d)). This transition point is 5 K above the T_{CO} value for the bulk $La_{0.45}Ca_{0.55}MnO_3$ sample.[73,74,81] If we consider that the transition at 225 K for the 700 and 800 °C annealed samples is related to the T_{CO} of bulk $La_{0.45}Ca_{0.55}MnO_3$ (where its particle size in composite increases with the annealing temperature), then it is difficult to rationalize the observation for the 1000 °C annealed sample. Moreover, this consideration also fails to account for the similar transition temperature of the 700 and 800 °C samples. Interestingly, it is close to the reported ferromagnetic T_C = 230 K of the $LaMn_{0.5}Fe_{0.5}O_3$ thin film superlattice of 1/1 stacking, confirming the alternate layer ordering of Fe^{3+} and Mn^{3+}.[36] The B-site cation ordering for $LaFe_{0.5}Mn_{0.5}O_3$ perovskites has not been reported yet in polycrystalline samples. In $La_{1-x}A_xFe_{0.5}Mn_{0.5}O_3$ (A = Ca, Sr and Pb; x = 0 & 0.25), neither the A-site radius nor the hole doping show a significant role in the magnetic properties, and all of the compositions fail to exhibit long-range ordering like $LaMn_{0.5}Fe_{0.5}O_3$.[57] There is also no evidence of long-range ordering in $La_{1-x}Ba_xFe_{0.5}Mn_{0.5}O_3$ (x = 0.25, 0.33 and 0.50).[58] However, the rhombohedral ($R\bar{3}c$) $Bi_{0.5}La_{0.5}Mn_{0.5}Fe_{0.5}O_3$ and $Bi_{0.5}Sr_{0.5}Mn_{0.5}Fe_{0.5}O_3$ exhibit canted antiferromagnetic ordering at 220 K and 226 K, respectively, due to the ordering of Fe^{3+} and Mn^{3+}/Mn^{4+}.[81] The interaction between Fe^{3+} and Mn^{4+} is weakly ferromagnetic based on the

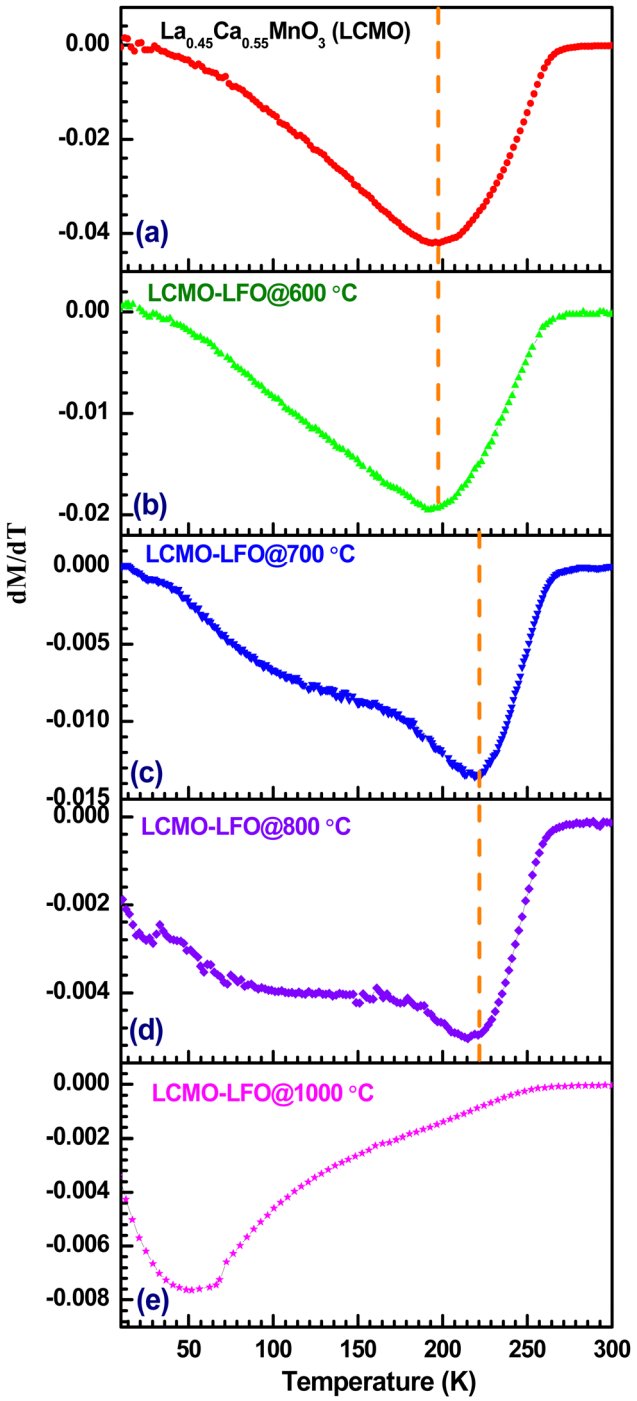

Fig. 12 Temperature derivative (dM/dT) of the FC magnetization as a function of temperature for $La_{0.45}Ca_{0.55}MnO_3$ (LCMO) (a) and LCMO–LFO composite annealed at: (b) 600 °C, (c) 700 °C, (d) 800 °C and (e) 1000 °C. The vertical lines indicate the minima corresponding to the T_C values.

Goodenough–Kanamori rule.[37] However, an antiferromagnetic ordering of Fe^{3+} and Mn^{4+} below 226 K is reported in $Bi_{0.5}Sr_{0.5}Mn_{0.5}Fe_{0.5}O_3$.[81] The magnetic property is also sensitive to the sample preparation condition.[81] This contrasting behaviour of the Bi content composition has been ascribed to the stereochemically active $6s^2$ lone pair of Bi^{3+}, which influences the structure, as well as the physical properties.[81,82] The above discussion and consideration of our observed magnetic data lead us to conclude that the possible ordering of $Fe^{3+}(d^5)$ and $Mn^{3+}(d^4)/Mn^{4+}(d^3)$ takes place across the interface of $La_{0.45}Ca_{0.55}MnO_3$ and $LaFeO_3$ nanoparticles with the formation of $La_{0.725}Ca_{0.275}Mn_{0.5}Fe_{0.5}O_3$. The possible superexchange interactions are Fe^{3+}–O–Fe^{3+}, Mn^{3+}–O–Mn^{3+}, Mn^{4+}–O–Mn^{4+}, Fe^{3+}–O–Mn^{3+} and Fe^{3+}–O–Mn^{4+}. According to the Goodenough–Kanamori rules, the Fe^{3+}–O–Mn^{4+} interaction is ferromagnetic, whereas other interactions are antiferromagnetic in nature.

The above claim on the temperature-controlled cation ordering in the product phase of the topotactic interface reaction is strongly substantiated by the formation of the B-site ordered double perovskite La_2MnCoO_6 across the interface of the $LaMnO_3$ and $LaCoO_3$ perovskite nanocomposite. $LaMnO_3$ is an antiferromagnetic insulator with $T_N \sim 140$ K.[83] The rhombohedral $R\bar{3}c$ phase of $LaCoO_3$ exhibits a spin state transition over a wide temperature range.[84,85] On the other hand, the monoclinic $P2_1/n$ phase of La_2MnCoO_6 with an ordered stacking of the B-site Mn^{4+} and Co^{2+}exhibits a ferromagnetic transition at $T_C = 225$ K.[42] However, the orthorhombic *Pbnm* phase with a random distribution of B-site cations has $T_C \sim 150$ K, along with the spin glass-type behavior at low temperature.[42,49,86,87] In the present investigation, we have also prepared nanocomposites with the ratio of 1 : 1 of $LaMnO_3$ and $LaCoO_3$, *i.e.*, LMO–LCO, and these were annealed at four different temperatures under a similar condition to that used for the LCMO–LFO nanocomposite discussed in the preceding sections. The XRD patterns for the LMO–LCO series of samples are shown in Fig. S9 (ESI†), confirming the purity of the phases. $LaMnO_3$ and $LaCoO_3$ were prepared at 500 °C by sol–gel method. Fig. 13 shows the temperature-dependent ZFC-FC magnetization, temperature derivative (dM/dT) curves and isothermal magnetization curves measured at 3 K for LMO–LCO composites annealed at 600, 700, 800 and 1000 °C. The magnetization curve of the 600 °C annealed sample in Fig. 13(a) shows the typical magnetization behaviour observed for both the $LaMnO_3$[88,89] and $LaCoO_3$ nanoparticles.[90,91] The dM/dT curve shows a minimum at ~80 K and a hysteresis loop of the typical ferromagnetic feature. This can be related to the surface ferromagnetism of the nanoparticles. This practically suggests no occurrence of a significant interface reaction across the grain boundary of $LaMnO_3$ and $LaCoO_3$.

The increase in annealing temperature to 700 °C and above in the ZFC-FC magnetization curves shown in Fig. 13(b)–(d) resembles the typical behaviour reported for La_2MnCoO_6.[42,49,86,87] There is a huge increase in magnetic transition temperature from 80 K for the 600 °C annealed LMO–LCO to 200 K for the 700 °C annealed sample (Fig. 13(b)). Furthermore, the onset of ferromagnetic transitions are 220 and 210 K for the 800 and 1000 °C annealed samples, respectively (Fig. 13(c) and (d)). The transition temperatures are determined from the minima in the dM/dT curves shown in the middle panel of Fig. 13. A slight decrease in T_C for the 1000 °C annealed sample

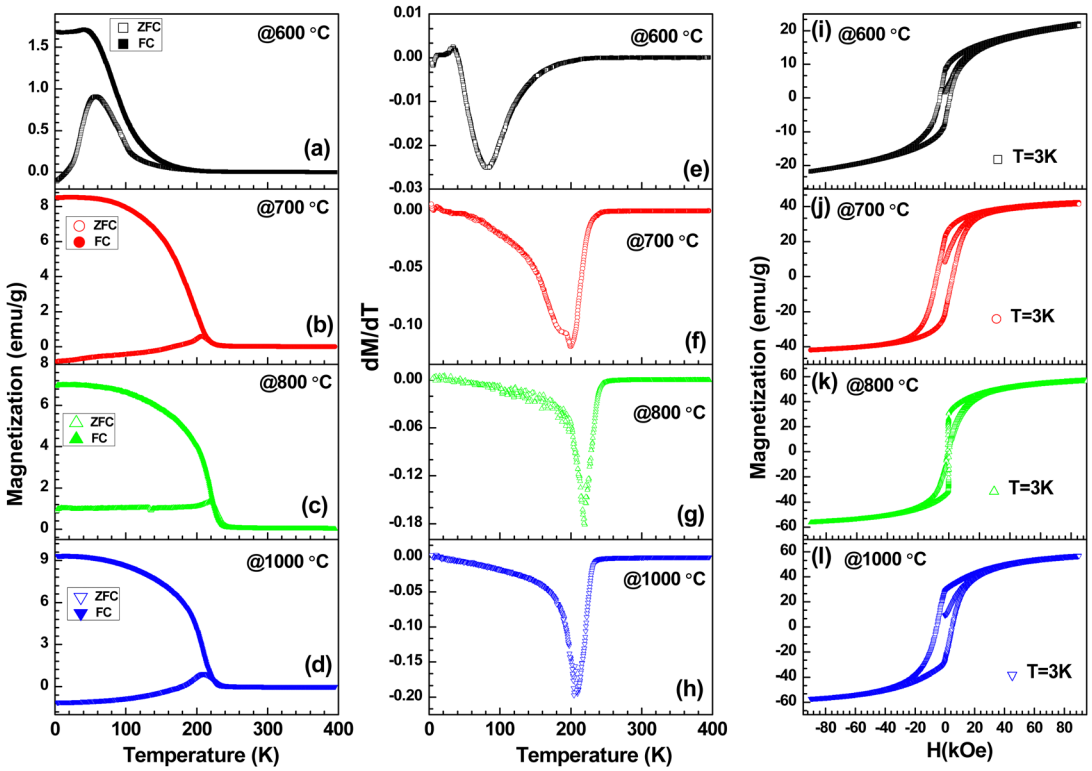

Fig. 13 Temperature-dependent magnetization ((a)–(d)), temperature derivative, dM/dT ((e)–(h)) and field-dependent isothermal magnetization, $M(H)$ ((i)–(l)) of $LaMnO_3$–$LaCoO_3$ (LMO–LCO) composite annealed at 600, 700, 800 and 1000 °C.

may be related to the anti-site disordering effect in La_2MnCoO_6.[42,49,86,87] The isothermal magnetization curves shown in Fig. 13(j)–(l) are in corroboration with the reported hysteresis loops for La_2MnCoO_6.[42,49,86,87] This result can be only be rationalized to the formation of cation-ordered La_2MnCoO_6 through the topotactic reaction at the interface of the grain boundaries between $LaMnO_3$ and $LaCoO_3$. The ferromagnetic transition observed is associated with the Mn^{4+}–O–Co^{2+} super-exchange interaction.

Conclusions

In summary, we have investigated the temperature evolution of the topotactic reaction across the grain boundary of the perovskite nanocomposites $La_{0.45}Ca_{0.55}MnO_3$–$LaFeO_3$ (LCMO–LFO) and $LaMnO_3$–$LaCoO_3$ (LMO–LCO). The pristine nanostructured oxides, as well as their composites, were characterized by PXRD, FE-SEM, EDX, elemental mapping, as well as TEM, EDX, ED and HAADF-STEM, XPS and magnetization measurements. The well-known charge ordered antiferromagnetic manganite $La_{0.45}Ca_{0.55}MnO_3$ in its nano-dimension exhibits surface ferromagnetism due to the relaxation of super-exchange at the surface. Similarly, the nanostructured antiferromagnetic $LaFeO_3$ (T_N ~740 K) also exhibits weak ferromagnetism due to inner spin canting, as well as surface effect. The magnetic property of the LCMO–LFO nanocomposite is dominated by the contribution of the $La_{0.45}Ca_{0.55}MnO_3$ phase at 600 °C annealing. The magnetic property of the LCMO–LFO composite is sensitive to the annealing temperature. TEM (HAADF-STEM), EDX-STEM elemental mapping confirms the formation of the intergrowth phase at lower temperature with a possible ordering of the cation, which was completely randomized at higher temperature. The LCMO–LFO composite clearly demonstrates the progressive dominance of the interface reaction product phase on magnetic properties of the composite system depending on the processing temperature. It revealed the cationic ordering in the product phase formed at lower temperatures. Accordingly, for the first time, we observed the Mn and Fe ordering in the product phase for the 700 and 800 °C annealed samples, where the observed T_C ~225 K is in good agreement with the reported value of 230 K in the 1 : 1 superlattice of $LaMnO_3/LaFeO_3$ with ordered Mn and Fe. The low temperature ordering of Mn and Fe is completely randomized by annealing at 1000 °C, resulting in a lack of magnetic ordering as observed in the bulk $La_{1-x}A_xFe_{0.5}Mn_{0.5}O_3$ perovskites. The temperature-controlled cationic ordering in the interfacial product phase formed by topotactic reaction with tunable magnetic property is substantiated by the formation of the well-known Mn and Co ordered double perovskite La_2MnCoO_6. The $LaMnO_3$–$LaCoO_3$ nanocomposite annealed at 800 °C results in the interface product phase with ferromagnetic T_C = 220 K, which is in agreement with the reported value of La_2MnCoO_6, confirming the cationic ordering. The high-resolution electron microscope study supports the temperature-controlled inter-growth phase formation with

cation ordering, as suggested from magnetic studies. We believe that the temperature-controlled cationic ordering through topotactic reaction at the interface of the nanocomposite with tunable magnetic properties will provide a strategic route to design functional ceramic materials.

Conflicts of interest

There are no conflicts to declare.

Acknowledgements

The authors gratefully acknowledge financial support from the Science and Engineering Research Board (SERB), Government of India, by a grant No: CRG/2021/000342 to Md. M. Seikh. M. Vasundhara would like to acknowledge the support offered by SERB grant number, CRG/2019/01574 and Department of K&IM of Indian Institute of Chemical Technology (IICT/Pubs./2024/097).

References

1 J. Zhang, R. J. Perez and E. J. Lavernia, *J. Mat. Sci.*, 1993, **28**, 835–846.
2 K. Lin, M. Zeng, H. Chen, X. Tao, Y. Ouyang, Y. Du and Q. Peng, *Int. J. Mech. Sci.*, 2022, **231**, 107580.
3 W. Chen, W. Yu, C. Ma, G. Ma, L. Zhang and H. Wang, *J. Magnes. Alloy.*, 2022, **10**, 1457–1475.
4 C. Vahlas, I. W. Hall and I. Haurie, *Mater. Sci. Eng., A*, 1999, **259**, 269–278.
5 J. H. Perepezko, M. H. da Silva Bassani, J. S. Park, A. S. Edelstein and R. K. Everett, *Mater. Sci. Eng., A*, 1995, **195**, 1–11.
6 R. J. Arsenault, *Composites*, 1994, **25**, 540–548.
7 J. S. Park, J. Cho, B. Y. Hur and J. H. Perepezko, *Met. Mater. Int.*, 2007, **13**, 1–12.
8 J. E. Garay, U. Anselmi-Tamburini and Z. A. Munir, *Acta Mater.*, 2003, **51**, 4487–4495.
9 Y. Cui, F. Liang, Z. Yang, S. Xu, X. Zhao, Y. Ding and J. Liu, *ACS Appl. Mater. Interfaces*, 2018, **10**, 9203–9210.
10 J. S. Park and J. M. Kim, *Materials*, 2010, **3**, 264–295.
11 S.-K. Lin, C.-L. Cho and H.-M. Chang, *J. Electron. Mater.*, 2014, **43**, 204–211.
12 A. Babaei-Dehkordi, M. Soltanieh, M. Mirjalili, M. Asherloo and A. Mostafaei, *Materials*, 2023, **16**, 2267.
13 T. Sarkar, A. K. Raychaudhuri, A. K. Bera and S. M. Yusuf, *New J. Phys.*, 2010, **12**, 123026.
14 T. Sarkar, M. V. Kamalakar and A. K. Raychaudhuri, *New J. Phys.*, 2012, **14**, 033026.
15 D. Lahiri, S. Khalid, T. Sarkar, A. K. Raychaudhuri and S. M. Sharma, *J. Condens. Matter Phys.*, 2012, **24**, 336001.
16 L. Pagliari, M. Dapiaggi, F. Maglia, T. Sarkar, A. K. Raychaudhuri, T. Chatterji and M. A. Carpenter, *J. Condens. Matter Phys.*, 2014, **26**, 435303.
17 J. Van Suchtelen, *Philips Res. Rep.*, 1972, **27**, 28–37.
18 C. W. Nan, M. I. Bichurin, S. Dong, D. Viehland and G. Srinivasan, *J. Appl. Phys.*, 2008, **103**, 031101.
19 H. Zheng, J. Wang, S. E. Lofland, Z. Ma, L. Mohaddes-Ardabili, T. Zhao, S. L. Riba, S. R. Shinde, S. B. Ogale, F. Bai and D. Viehland, *Science*, 2004, **303**, 661–663.
20 B. K. Bammannavar, L. R. Naik and B. K. Chougule, *J. Appl. Phys.*, 2008, **104**, 064123.
21 W. J. Feng, D. Geng, J. J. Ceng, J. Z. Sheng, S. Zhang and H. Yang, *Integr. Ferroelectr.*, 2011, **129**, 215–222.
22 G. Muscas, P. A. Kumar, G. Barucca, G. Concas, G. Varvaro, R. Mathieu and D. Peddis, *Nanoscale*, 2016, **8**, 2081–2089.
23 P. K. Manna and S. M. Yusuf, *Phys. Rep.*, 2014, **535**, 61–99.
24 T. P. Gavrilova, R. M. Eremina, I. V. Yatsyk, I. F. Gilmutdinov, A. G. Kiiamov, N. M. Lyadov and Y. V. Kabirov, *J. Alloys Compd.*, 2017, **714**, 213–224.
25 R. M. Eremina, K. R. Sharipov, I. V. Yatsyk, N. M. Lyadov, I. F. Gilmutdinov, A. G. Kiiamov, Y. V. Kabirov, V. G. Gavrilyachenko and T. I. Chupakhina, *J. Exp. Theor. Phys.*, 2016, **123**, 127–133.
26 A. Haque, D. Ghosh, U. Dutta, A. Shukla, A. Gayen, P. Mahata, A. K. Kundu and M. M. Seikh, *J. Magn. Magn. Mater.*, 2020, **494**, 165847.
27 T. Sarkar, G. Muscas, G. Barucca, F. Locardi, G. Varvaro, D. Peddis and R. Mathieu, *Nanoscale*, 2018, **10**, 22990–23000.
28 P. Maltoni, T. Sarkar, G. Barucca, G. Varvaro, D. Peddis and R. Mathieu, *J. Magn. Magn. Mater.*, 2021, **535**, 168095.
29 P. Maltoni, T. Sarkar, G. Barucca, G. Varvaro, F. Locardi, D. Peddis and R. Mathieu, *J. Phys. Chem. C*, 2021, **125**, 5927–5936.
30 F. Afzal, M. T. Ansar, A. S. Haidyrah, M. A. Khan, G. M. Mustsfa, M. Saleemand and S. Atiq, *J. Alloys Compd.*, 2021, **888**, 161516.
31 M. Zhang, M. Jia and Y. Jin, *Appl. Surf. Sci.*, 2012, **261**, 298–305.
32 H. Tabata, H. Tanaka and T. Kawai, *Appl. Phys. Lett.*, 1994, **65**, 1970–1972.
33 G. Q. Gong, A. Gupta, G. Xiao, P. Lecoeur and T. R. McGuire, *Phys. Rev. B: Condens. Matter Mater. Phys.*, 1996, **54**, R3742.
34 M. Yoshimoto, H. Nagata, S. Gonda, J. P. Gong, H. Ohkubo and H. Koinuma, *Phys. C*, 1991, **190**, 43–45.
35 P. C. Rout, A. Ray and U. Schwingenschlögl, *Npj Comput. Mater.*, 2023, **9**, 165.
36 K. Ueda, H. Tabata and T. Kawai, *Phys. Rev. B: Condens. Matter Mater. Phys.*, 1999, **60**, R12561.
37 J. Kanamori, *J. Phys. Chem. Solids*, 1959, **10**, 87–98.
38 J. B. Goodenough, *Phys. Rev.*, 1955, **100**, 564.
39 J. B. Goodenough, A. Wold, R. J. Arnott and N. J. P. R. Menyuk, *Phys. Rev.*, 1961, **124**, 373.
40 G. Blasse, *J. Phys. Chem. Solids*, 1965, **26**, 1969–1971.
41 U. Dutta, O. I. Lebedev, A. K. Kundu and M. M. Seikh, *J. Phys.: Condens. Matter*, 2019, **32**, 085803.
42 A. Haque, R. Das, D. Ghosh, M. Vasundhara, A. Gayen, A. K. Kundu and M. M. Seikh, *J. Phys. Chem. C*, 2021, **125**, 3088–3101.
43 K. De, R. Ray, R. N. Panda, S. Giri, H. Nakamura and T. Kohara, *J. Magn. Magn. Mater.*, 2005, **288**, 339–346.

44 O. F. De Lima, J. A. H. Coaquira, R. L. de Almeida and S. K. Malik, *J. Appl. Phys.*, 2010, **107**, 09E107.
45 K. De, M. Thakur, A. Manna and S. Giri, *J. Appl. Phys.*, 2006, **99**, 013908.
46 U. Dutta, D. Ghosh, A. Haque, L. Kumar, T. K. Mandal, P. S. Walke, K. Pal, A. Gayen, A. K. Kundu and M. M. Seikh, *J. Phys.: Condens. Matter*, 2019, **31**, 225801.
47 Y. Sun, W. Tong, X. Xu and Y. Zhang, *Phys. Rev. B: Condens. Matter Mater. Phys.*, 2001, **63**, 174438.
48 D. V. Karpinsky, I. O. Troyanchuk and V. V. Sikolenko, *J. Phys.: Condens. Matter*, 2007, **19**, 036220.
49 A. Haque, R. Das, D. Ghosh, O. I. Lebedev, A. Gayen, A. K. Kundu and M. M. Seikh, *J. Magn. Magn. Mater.*, 2020, **514**, 167159.
50 R. Das, S. Bhattacharya, A. Haque, D. Ghosh, O. I. Lebedev, A. Gayen and M. M. Seikh, *J. Magn. Magn. Mater.*, 2021, **538**, 168267.
51 V. Solanki, S. Das, S. Kumar, M. M. Seikh, B. Raveau and A. K. Kundu, *J. Sol-Gel Sci. Technol.*, 2017, **82**, 536–540.
52 V. Solanki, M. M. Seikh and A. K. Kundu, *J. Magn. Magn. Mater.*, 2019, **469**, 95–99.
53 D. Ghosh, R. Das, A. Haque, K. Ghorai, A. Gayen, P. Mahata, A. K. Kundu and M. M. Seikh, *J. Magn. Magn. Mater.*, 2021, **523**, 167621.
54 X. D. Zhou, L. R. Pederson, Q. Cai, J. Yang, B. J. Scarfino, M. Kim, W. B. Yelon, W. J. James, H. U. Anderson and C. Wang, *J. Appl. Phys.*, 2006, **99**, 08M918.
55 K. Ramesha, V. Thangadurai, D. Sutar, S. V. Subramanyam, G. N. Subbanna and J. Gopalakrishnan, *Mater. Res. Bull.*, 2000, **35**, 559–565.
56 V. Joly, S. Bhame, P. Joy and S. Date, *J. Magn. Magn. Mater.*, 2003, **261**, 433.
57 A. Hossain, D. Ghosh, U. Dutta, P. S. Walke, N. E. Mordvinova, O. I. Lebedev, B. Sinha, K. Pal, A. Gayen, A. K. Kundu and M. M. Seikh, *J. Magn. Magn. Mater.*, 2017, **444**, 68–76.
58 U. Dutta, A. Hossain, P. S. Walke, D. Ghosh, N. E. Mordvinova, O. I. Lebedev, A. Haque, K. Pal, A. Gayen, A. K. Kundu and M. M. Seikh, *J. Alloys Compd.*, 2019, **777**, 1396–1402.
59 S. D. Bhame, V. J. Joly and P. A. Joy, *Phys. Rev. B: Condens. Matter Mater. Phys.*, 2005, **72**, 054426.
60 Z. X. Wei, Y. Wang, J. P. Liu, C. M. Xiao and W. W. Zeng, *Mater. Chem. Phys.*, 2012, **136**, 755–761.
61 P. Hao, P. Song, Z. Yang and Q. Wang, *J. Mater. Sci.: Mater. Electron.*, 2020, **31**, 4632–4641.
62 R. H. Blackmore, M. E. Rivas, G. F. Tierney, K. M. Mohammed, D. Decarolis, S. Hayama, F. Venturini, G. Held, R. Arrigo, M. Amboage, P. Hellier, E. Lynch, M. Amri, M. Casavola, T. E. Erden, P. Collier and P. P. Wells, *Phys. Chem. Chem. Phys.*, 2020, **22**, 18774–18787.
63 B. Poojitha, R. Shukla, M. Vasundhara, U. M. Rasi, R. B. Gangineni, S. C. Sahoo, R. J. Choudhary, Y. Bitla and A. K. Patra, *J. Magn. Magn. Mater.*, 2021, **530**, 167851.
64 T. Vijayaraghavan, R. Sivasubramanian, S. Hussain and A. Ashok, *Chemistry Select*, 2017, **2**, 5570–5577.
65 B. Arun, V. R. Akshay and M. Vasundhara, *Dalton Trans.*, 2018, **47**, 15512–15522.
66 A. Haque, R. Das, M. Vasundhara, D. Ghosh, A. Gayen, P. Mahata, A. K. Kundu and M. M. Seikh, *J. Alloys Compd.*, 2021, **875**, 159984.
67 A. P. B. Selvadurai, V. Pazhanivelu, C. Jagadeeshwaran, R. Murugaraj, I. P. Muthuselvam and F. C. Chou, *J. Alloys Compd.*, 2015, **646**, 924–931.
68 M. R. Todd, L. C. Gary and M. A. James, *Phys. Rev. B: Condens. Matter Mater. Phys.*, 1993, **48**, 224–238.
69 E. K. Abdel-Khalek, I. Ibrahim and T. M. Salama, *Ferroelectrics*, 2019, **550**, 210–219.
70 Y. Qiu, Y. S. Luo, Z. J. Zou, Z. M. Tian, S. L. Yuan, Y. Xi and L. Z. Huang, *J. Mater. Sci.: Mater. Electron.*, 2014, **25**, 760–764.
71 S. Phokha, S. Pinitsoontorn, S. Maensiri and S. Rujirawat, *J. Sol-Gel Sci. Technol.*, 2014, **71**, 333–341.
72 A. A. Cristóbal, P. M. Botta, E. F. Aglietti, M. S. Conconi, P. G. Bercoff and J. P. López, *Mater. Chem. Phys.*, 2011, **130**, 1275–1279.
73 Y. Tokura, *Colossal magnetoresistive oxides*, CRC Press, 2000.
74 R. Schmidt, *Phys. Rev. B: Condens. Matter Mater. Phys.*, 2008, **77**, 205101.
75 T. Sarkar, B. Ghosh, A. K. Raychaudhuri and T. Chatterji, *Phys. Rev. B: Condens. Matter Mater. Phys.*, 2008, **77**, 235112.
76 B. Samantaray, S. K. Srivastava and S. Ravi, *J. Appl. Phys.*, 2012, **111**, 013919.
77 S. S. Rao, S. Tripathi, D. Pandey and S. V. Bhat, *Phys. Rev. B: Condens. Matter Mater. Phys.*, 2006, **74**, 144416.
78 T. Zhang, T. F. Zhou, T. Qian and X. G. Li, *Phys. Rev. B: Condens. Matter Mater. Phys.*, 2007, **76**, 174415.
79 K. Das, D. Mazumdar, P. Dasgupta, S. Kumar and I. Das, *J. Magn. Magn. Mater.*, 2021, **528**, 167804.
80 P. Schiffer, A. P. Ramirez, W. Bao and S. W. Cheong, *Phys. Rev. Lett.*, 1995, **75**, 3336.
81 P. Mandal, S. S. Bhat, Y. Sundarayya, A. Sundaresan, C. N. R. Rao, V. Caignaert, B. Raveau and E. Suard, *RSC Adv.*, 2012, **2**, 292–297.
82 R. Seshadri and N. A. Hill, *Chem. Mater.*, 2001, **13**, 2892–2899.
83 T. Chatterji, P. F. Henry and B. Ouladdiaf, *Phys. Rev. B: Condens. Matter Mater. Phys.*, 2008, **77**, 212403.
84 B. Raveau and M. M. Seikh, *Cobalt oxides: from crystal chemistry to physics*, John Wiley & Sons, 2012.
85 M. M. Seikh, L. Sudheendra, C. Narayana and C. N. R. Rao, *J. Mol. Struct.*, 2004, **706**, 121–126.
86 R. I. Dass and J. B. Goodenough, *Phys. Rev. B: Condens. Matter Mater. Phys.*, 2003, **67**, 014401.
87 P. A. Joy, Y. B. Khollam and S. K. Date, *Phys. Rev. B: Condens. Matter Mater. Phys.*, 2000, **62**, 8608.
88 P. Tiwari and C. Rath, *J. Magn. Magn. Mater.*, 2017, **441**, 635–641.
89 P. Tiwari and C. Rath, *AIP Conf. Proc.*, 2017, **1832**, 050099.
90 S. Zhou, L. He, S. Zhao, Y. Guo, J. Zhao and L. Shi, *J. Phys. Chem. C*, 2009, **113**, 13522–13526.
91 Q. Wei, T. Zhang, X. P. Wang and Q. F. Fang, *Eur. Phys. J.: Appl. Phys.*, 2012, **57**, 30401.